

# Imaging over an unlimited bandwidth with a single diffractive surface

*Sourangsu Banerji,<sup>1,\*</sup> Monjurul Meem,<sup>1,\*</sup> Apratim Majumder,<sup>1</sup> Berardi Sensale-Rodriguez<sup>1</sup> and Rajesh Menon<sup>1, 2, a)</sup>*

<sup>1</sup>Department of Electrical and Computer Engineering, University of Utah, Salt Lake City, UT 84112, USA.

<sup>2</sup>Oblate Optics, Inc. San Diego CA 92130, USA.

a) [rmenon@eng.utah.edu](mailto:rmenon@eng.utah.edu)

\* Equal contribution.

## ABSTRACT

It is generally thought that correcting chromatic aberrations in imaging requires multiple surfaces. Here, we show that by allowing the phase in the image plane of a flat lens to be a free parameter, it is possible to correct chromatic aberrations over an almost unlimited bandwidth with a single diffractive surface. Specifically, we designed, fabricated and characterized a flat multi-level diffractive lens (MDL) that images at the wavelengths from 450nm to 850nm. We experimentally characterized the focusing efficiency, modulation-transfer function, wavefront aberrations, vignetting, distortion and signal-to-noise ratio performance of a camera comprised of this MDL and a conventional image sensor. Further, we designed two MDLs with operating wavelengths from 500nm to 15 $\mu$ m, and from 2 $\mu$ m to 150 $\mu$ m, respectively. With no apparent limitation in the operating bandwidth, such flat lenses could replace multiple refractive surfaces that are traditionally required for chromatic corrections, leading to thinner, lighter and simpler imaging systems with bandwidth limited primarily by the quantum efficiency of the sensor.

## Introduction

The lens is considered the most fundamental element for imaging. Imaging is information transfer from the object to the image planes. This can be accomplished via a conventional lens that essentially performs a one-to-one mapping [1], via an unconventional lens (such as one with a structured point-spread function or PSF) that performs a one-to-many mapping, or via no lens, where the light propagation essentially performs a one-to-all mapping. In the first case, the image is formed directly. In the second case, the image is formed after a computation and can be useful, when encoding spectral [2-3] or depth [4] or polarization [5] or other information into the geometry of the PSF itself. Note that the modification of the PSF may be at the same scale as the diffraction limit [2-5] or it can even be much larger [6-9]. The image can be recovered in many cases in the optics-less scenario as well [10,11], but more importantly, machine learning may be employed to make inferences based on the acquired information (even without performing image reconstruction for human visualization), which has potential implications for privacy among other interesting outcomes [12]. However, the conventional lens approach is preferred in many cases due to the high signal-to-noise ratio achievable at each image pixel (resulting from the 1:1 mapping). When this conventional lens is illuminated by a plane wave, it forms a focused spot at a distance equal to its focal length.

Now, if we appeal to the fact that in the vast majority of imaging applications, only the intensity is measured, the phase of the field in the image or focal plane is a free parameter, something which comes from the inverse diffraction transform [13]. Then, it is easy to see that the phase of the plane wave after it transmits the lens can have multiple forms. We extended this concept to a continuous spectrum of wavelengths from 450nm to 850nm, and designed a single Multi-level Diffractive Lens (MDL) with focal length of 1mm and aperture of 150 $\mu$ m, whose schematic is shown in Fig. 1A. The MDL has a fixed geometry as illustrated in Fig. 1B. However, its material dispersion and wavelength determine the phase transmittance function as shown in Figs. 1C-F for  $\lambda=500$ nm, 600nm, 700nm and 800nm, respectively. When these phase distributions are propagated to the focal plane (1mm away), we obtain the phase, amplitude and intensity distributions at  $\lambda =500$ nm (Figs. 1G-I), 600nm (Figs. 1J-L), 700nm (Figs. 1M-O) and 800nm (Figs. 1P-R), respectively. Note that the intensity distributions for all the four wavelengths are

almost identical, but their phase distributions are quite different. This example, as well as our argument above simply shows that the lens does not possess a *unique* phase transmittance function. This is in contradiction to most textbooks that teach us that the ideal lens should have a parabolic phase profile. By removing this restriction, we enable numerous solutions to the ideal lens. Then, the final choice can be made based upon other requirements such as achromaticity, minimization of aberrations, manufacturability, etc. Stating this differently, we can show that a single surface can correct chromatic and other imaging aberrations, something that was considered impossible in refractive lenses [14]. In fact, we show that the achievable bandwidth is in fact unlimited for practical purposes. In this paper, we experimentally demonstrate such an example of a single surface, whose phase-transmittance function is engineered to minimize chromatic aberrations over a bandwidth of 450nm to 850nm. We further show via simulations two separate MDLs, each representing a single surface that is engineered to focus light from  $\lambda = 0.5\mu\text{m}$  to  $15\mu\text{m}$ , and from  $\lambda = 2.5\mu\text{m}$  to  $150\mu\text{m}$ , respectively.

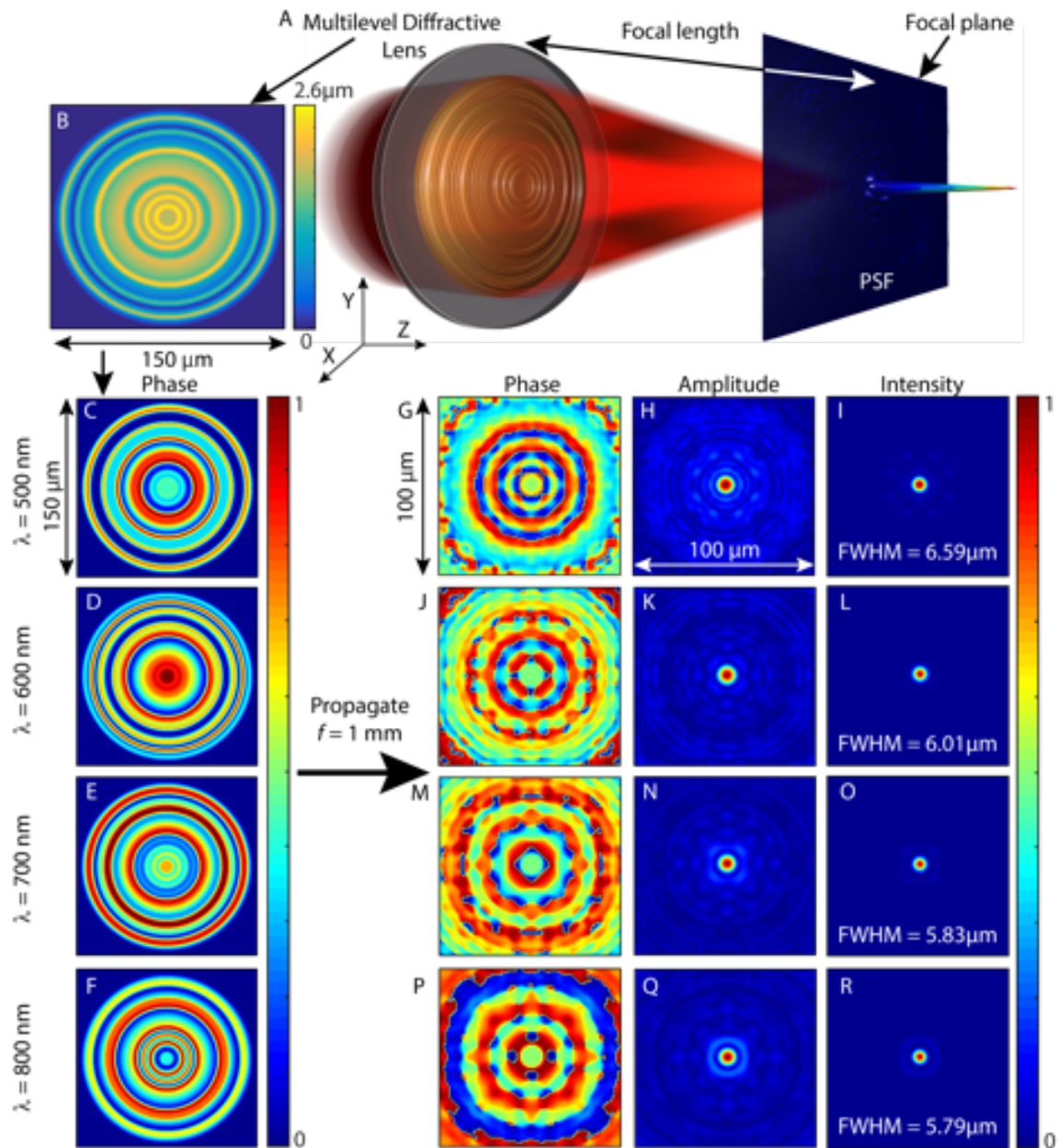


**Figure 1:** (A) Schematic of a single surface multi-level diffractive lens (MDL) that performs close to 1:1 mapping over a broad spectrum. (B) Topography of an MDL with focal length=1mm, aperture=150μm and operating wavelengths from 450nm to 850nm. The minimum feature width, maximum feature height and number of levels for this MDL are 3μm, 2.6μm and 100, respectively. (C) Phase distribution in the MDL plane at  $\lambda = 500\text{nm}$ . (D-F) The amplitude, phase and intensity distributions in the focal plane for  $\lambda = 500\text{nm}$ . The corresponding plots for  $\lambda = 600\text{nm}$ ,  $700\text{nm}$  and  $800\text{nm}$  are shown in (G-R). The phase is normalized to  $2\pi$  and amplitude and intensity are normalized to their maximum values in all plots. Note that the intensity distributions are almost identical for all four wavelengths, but their phase distributions are quite different. Achromaticity with a single surface is achieved by allowing phase in the focal plane to be a free parameter.

It is important to note that in conventional refractive imaging systems, multiple lenses (sometimes made from different materials with differing dispersion properties) are used to correct for chromatic aberrations [14]. Not only are the individual refractive lenses thick and heavy, but multiple lenses require precise alignment during assembly. Metalenses have recently become popular to mitigate these disadvantages. By engineering deep subwavelength features on a surface, the parabolic phase profile with group-velocity compensation has been applied to correct for chromatic aberrations [15]. Via a careful literature study (see Table S1) [16], we conclude that the best achromatic metalens in the visible band has demonstrated efficiency of about 35% from 460nm to 700nm for unpolarized light [15]. However, this metalens requires 50nm-wide, 600nm-tall structures in TiO<sub>2</sub> because high refractive index is necessary for its operation. Needless to say, no metalens to date has ever reported polarization-insensitive imaging with high efficiency over the visible and near-IR bands. In fact, we recently showed that appropriately designed multi-level diffractive lenses (MDLs) are not only far easier to fabricate, but they outperform most metalenses, and thereby concluded that metalenses do not offer any advantage for imaging [17]. We have already demonstrated MDLs in the visible (450nm to 750nm) [18, 19], coupling two MDLs for magnification, [20], in the long-wave infrared (8 $\mu$ m to 12 $\mu$ m) [21] and in the terahertz band (1 mm to 3 mm) [22, 23].

In this paper, we exploit the concept of non-unique lens phase functions to experimentally demonstrate MDLs with high efficiency over the visible and near-infrared bands (450nm to 850nm) utilizing relatively large microstructures (3 $\mu$ m wide, 2.6 $\mu$ m tall) fabricated in a polymer. Furthermore, we show via simulations two different MDLs with an even more extended operation bandwidth, one that is achromatic from 0.5 $\mu$ m to 15 $\mu$ m and second from 2 $\mu$ m to 150 $\mu$ m.

## **Design**

The details of our design methodology have been reported before [18-23]. To summarize, we maximize the wavelength-averaged focusing efficiency of the MDL by selecting the distribution of heights of the rings that form the MDL (see Fig. 1A). This selection is based upon a modified direct binary search technique. We designed, fabricated and characterized an MDL with focal length and NA of 1mm and 0.075,

respectively operating at the wavelength range of 450nm to 850nm. The design had a constraint of at most 100 height levels with a maximum individual height level of 2.6 $\mu$ m and minimum feature width of 3 $\mu$ m. The material dispersion of a positive-tone photoresist, S1813 (Microchem) (Fig. S1) was assumed [16]. The height distribution of the designed MDL is shown in Fig. 1B, while the phase transmittance function at four wavelengths are shown in Figs. 1C-F. As mentioned earlier, when these fields are propagated to the focal plane, 1mm away from the MDL, the resulting amplitude and phase distributions as well as the intensity distributions at the corresponding wavelengths are shown in Fig. 1. Note that even though the phase distribution in the focal plane differs between the wavelengths, the intensity distributions are almost identical to that expected from the diffraction-limited case. As a result, we have a single-surface lens that is achromatic from 450nm to 850nm. The simulated PSFs for all the wavelengths are depicted in Fig. S4 [16].

## Experiments

The MDL was fabricated using grayscale lithography as has been reported previously (Fig. S6) [16,18-21]. An optical micrograph of the fabricated device is shown in Fig. 2A. The point-spread function (PSF) of the MDL was measured by illuminating it by a collimated beam from a tunable supercontinuum source (NKT Photonics SuperK Extreme with SuperK VARIA filter for visible wavelengths, 350nm-850nm and SuperK SELECT filter for near infrared wavelengths, 800nm-1400nm) (Fig. S7) [16, 18-20]. The wavelength of the source was tuned from 450nm to 850nm in steps of 50 nm and bandwidth of 10 nm. The focused spot at each wavelength was relayed with magnification (22.22X) onto a monochrome image sensor (DMM 27UP031-ML, Imaging Source). The captured raw images for four wavelengths are shown in Figs. 2B-E, where we note all the wavelengths are close to focus, exhibiting achromatic behavior. The full-width at half-maximum (FWHM) of the measured PSFs are noted in the corresponding images. The diffraction-limited, measured and simulated FWHM as function of wavelength are plotted in Fig. 2F, which shows good agreement. The measured PSFs for all the wavelengths are shown in Fig. S5 [16].

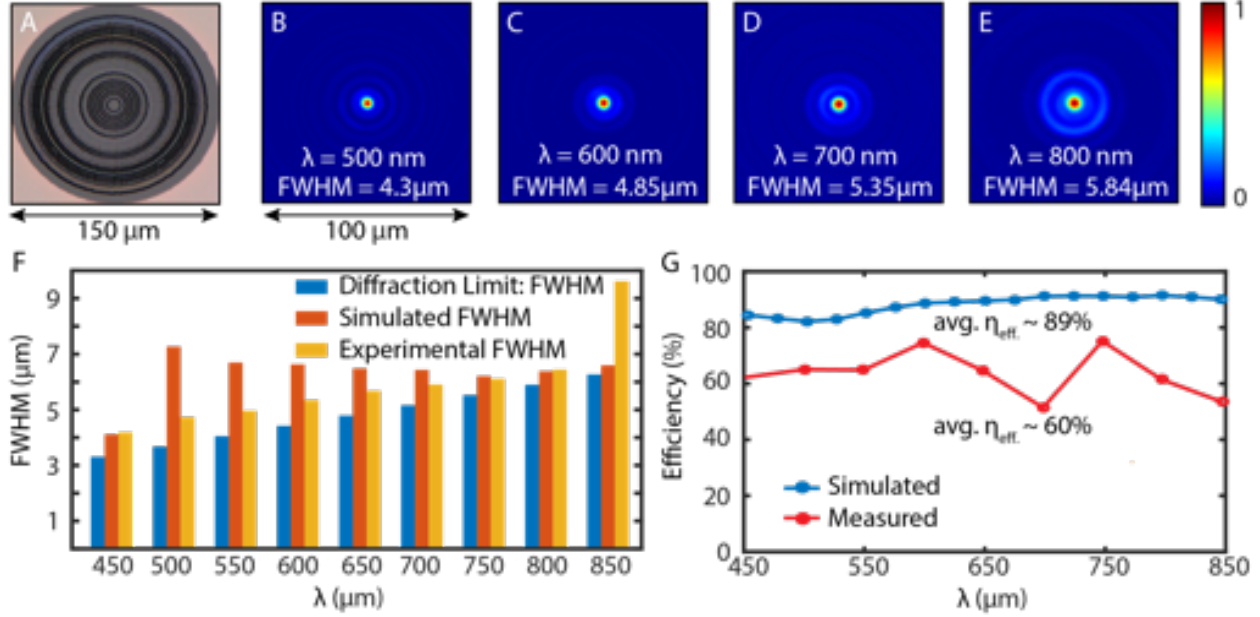


**Figure 2:** Achromatic focusing by the MDL. (A) Optical micrograph of the fabricated MDL. (B-E) Measured point-spread functions at the same focal plane, 1mm away from the MDL at four wavelengths. (F) Measured, simulated and diffraction-limited full-width at half-maximum (FWHM) as function of wavelength. (G) Measured and simulated focusing efficiency as a function of wavelength. The operating bandwidth of the MDL is 450nm to 850nm.

The focusing efficiency of the MDL (Fig. 2G) is calculated as the power within a spot of diameter equal to 3 times the FWHM divided by the total power incident on the lens [16, 24]. The simulated wavelength averaged focusing efficiency for the designed MDL is  $\sim 89\%$  in comparison to a measured value of  $\sim 60\%$  in the 450 nm to 850 nm band. In order to explain this discrepancy, we performed careful simulations of the sensitivity of the focusing efficiency to errors in the ring heights (Fig. S8) and ring widths (Fig. S9) [16]. The analysis suggests that standard deviation in ring heights of 100nm coupled with standard deviation in ring widths of about 150nm can explain the drop in efficiency (Fig. S11). Such standard deviations are expected in our existing grayscale lithography process (see Fig. S10 for error measurements). In the future, it is possible to incorporate tolerance to fabrication errors as one of the metrics during the optimization-based design step, analogous to what was done previously for binary multi-wavelength diffractive lenses [25].

Next, we assembled a camera by placing the MDL in front of a conventional image sensor (Fig. 3A). Then, we characterized the imaging behavior of the MDL by capturing still and video images of the

Air Force resolution target (450nm to 850nm in Fig. 3B and illumination spectrum in Fig. S18) and the Macbeth color chart (visible in Fig. 3C and in Supplementary Video 1, and NIR in Fig. 3D and in Supplementary Video 2) [16]. The distance between the MDL and the image sensor was  $\sim 2.5$ mm, and the distance between the object and the MDL was  $\sim 1.7$ mm. The visible and NIR frames were captured using a color image sensor (DFM 72BUC02-ML, Imaging Source). In each case, the exposure time was adjusted to ensure that the frames were not saturated. In addition, a dark frame was recorded and subtracted from the images. The resolution-chart image shows that the resolved spatial frequency is  $\sim 144$  line-pairs/mm, which corresponds to a spatial period of  $6.9\mu\text{m}$  or about 3 times the sensor pixel size ( $2.2\mu\text{m}$ ). This resolution corresponds approximately to the average FWHM over all the wavelengths in Fig. 2F. Finally, the visible image of the Macbeth color chart shows excellent color reproduction.

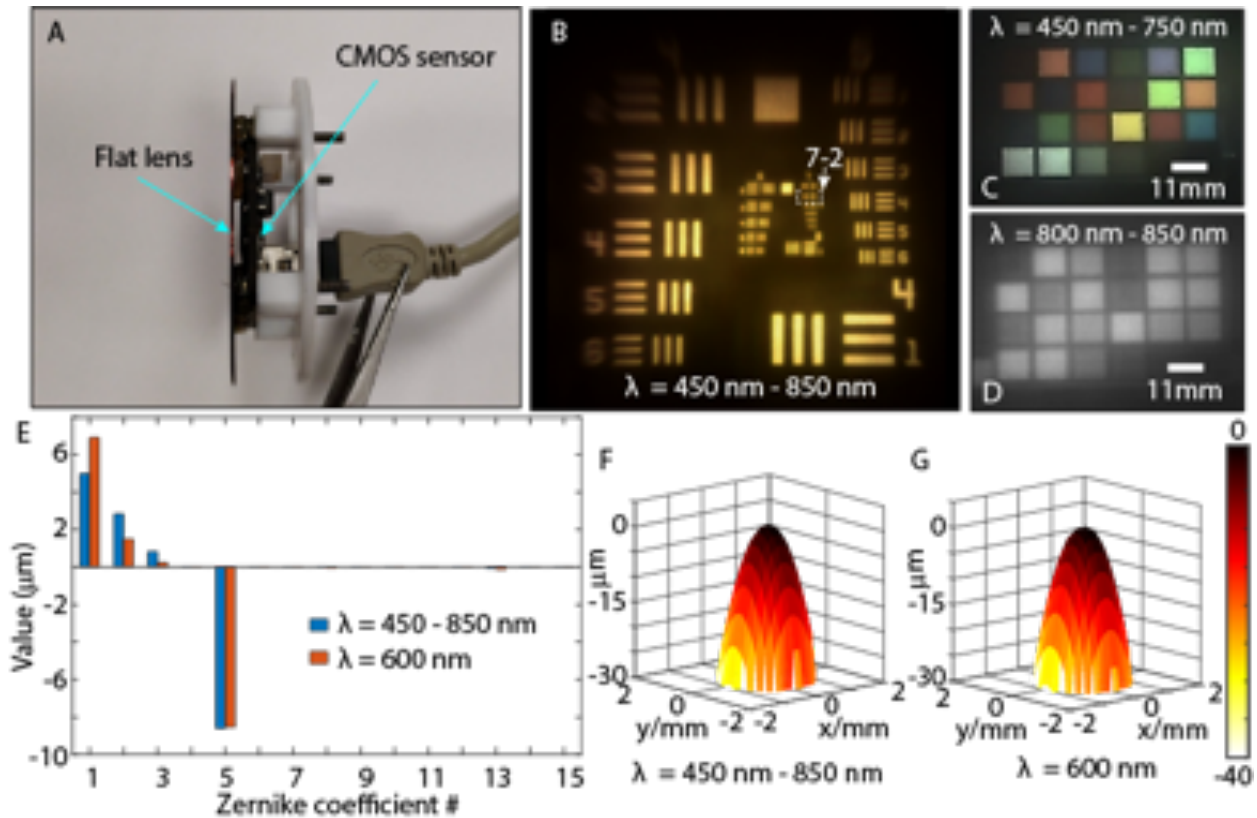


**Figure 3:** Imaging characterization of the MDL. (A) Photograph of the camera comprising a conventional image sensor and the MDL. (B) Image of the AirForce resolution chart under broadband (450nm to 850nm) illumination. Images of the Macbeth color chart under (C) visible (see Supplementary Video 1) and (D) near-IR illumination (see Supplementary Video 2). (E) Zernike aberrations coefficients measured using a Shack-Hartmann wavefront sensor for our MDL under broadband illumination and under 600nm



*illumination. Measured wavefront errors under (F) broadband and (G) narrowband illumination. Note that the distance between the MDL and the image sensor was fixed while taking the visible and NIR images.*

The wavefront aberrations of the fabricated MDL were measured using a Shack-Hartmann wavefront sensor (Thorlabs, WFS 150-7AR) [16]. The wavefront aberrations were measured under broadband (450nm to 850nm) and under narrowband illuminations at 600nm with 50 nm bandwidth. The corresponding Zernike polynomial coefficients are shown in Fig. 3E. The measurements confirm that the MDL indeed has low values for all aberrations (Table S2) [16]. Most importantly, the aberrations as well as the reconstructed wavefront are quite similar for both the broadband (Fig. 3F) and 600nm narrowband (Fig. 3G) illumination, confirming excellent achromaticity. We also simulated the aberrations for the MDL and these agree well with the experiments (Tables S3 and S4) [16].

Next, we calculated the modulation-transfer function (MTF) of the MDL by taking the absolute value of the Fourier transform of the captured PSFs. The extracted MTF plots are shown in Fig. 4A for all the wavelengths. The first zero crossing of the on-axis MTF at 10% contrast occurs between 130 to 140 line-pairs/mm for the visible wavelengths and about 60 line-pairs/mm for the NIR wavelengths. This is also quite consistent with the resolution limits estimated from the chart in Fig. 3. We furthered studied vignetting of the MDL (Fig. 4B) by photographing a uniform plane of white color, which was bigger than the field of view (FOV) of the MDL. This uniform white plane was illuminated from far by white LEDs. The normalized intensity across the MDL FOV with respect to its viewing angle gives us the vignetting performance of the MDL. For characterizing the geometric distortion of the MDL, we replaced the white plane with a regular checkered grid and measured the grid-point distortion percentage with respect to the MDL viewing angle. The results of the geometric distortion are shown in Figs. 4C and 4D in the vertical and horizontal directions, respectively. Low astigmatism is noted. Lastly, we measured the signal-to-noise ratio (SNR) response of the MDL when photographing uniform planes of red, green and blue colors (Figs. E-G, respectively) and confirm  $\text{SNR} > 40\text{dB}$  for all corresponding color channels. Our careful characterization shows that the performance of our MDL is comparable to that of thick refractive lens systems.

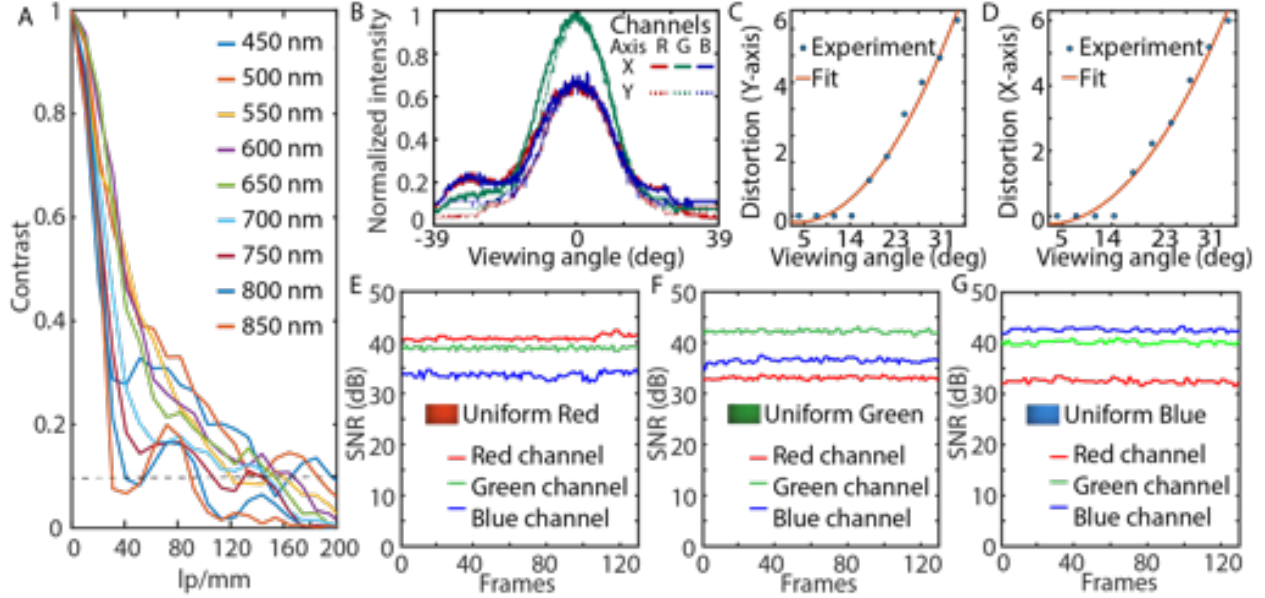


**Figure 4:** Analysis of the MDL. (A) Modulation-transfer-function (MTF) and (B) Vignetting measurement showing normalized intensity vs viewing angle in degrees. (C, D) Geometric distortion showing distortion of a regular geometric grid in the Y (C) and X (D) axes as a function of the viewing angle in degrees and (E-G) Signal-to-Noise Ratio (SNR) of the MDL when imaging a patch of uniform (E) Red, (F) Green and (G) Blue color for each of the Red, Green and Blue channels of the CMOS sensor.

### Extending the operating bandwidth

Extending the concept of phase in the focal plane as a free parameter, we can design a single MDL (one diffractive surface) to be achromatic over an even larger bandwidth. In Fig. 5A, we show the simulated focusing efficiency of a lens designed to focus  $\lambda=0.5\mu\text{m}$  to  $15\mu\text{m}$  at a single focal plane, 5mm away. The dispersion properties of photopolymer (AZ9260, Microchem) (Fig. S2) were assumed [16]. We have previously fabricated MDLs in the IR using this material [21]. Even though the photopolymer exhibits absorption in the IR, due to its drastically reduced thickness ( $10\mu\text{m}$ ), the lens exhibits focusing efficiency of 76% averaged over the entire wavelength range of  $0.5\mu\text{m}$  to  $15\mu\text{m}$ . The designed geometry of the lens is shown in Fig. 5B. The minimum feature width, maximum feature height and number of levels were  $6\mu\text{m}$ ,  $10\mu\text{m}$  and 100, respectively. The simulated point-spread functions at select wavelengths are shown in Figs. 5C-H (PSFs for all the wavelengths are shown in Fig. S19 [16]). We further confirmed that the simulated full-width at half-maximum approximately tracked the theoretical diffraction-limited values (Fig. S20)

[16]. In addition, we also performed a rigorous finite-difference time domain (FDTD) simulation of this MDL for select wavelengths to highlight the achromatic focusing in a 2D slice (Fig. S21) [16].

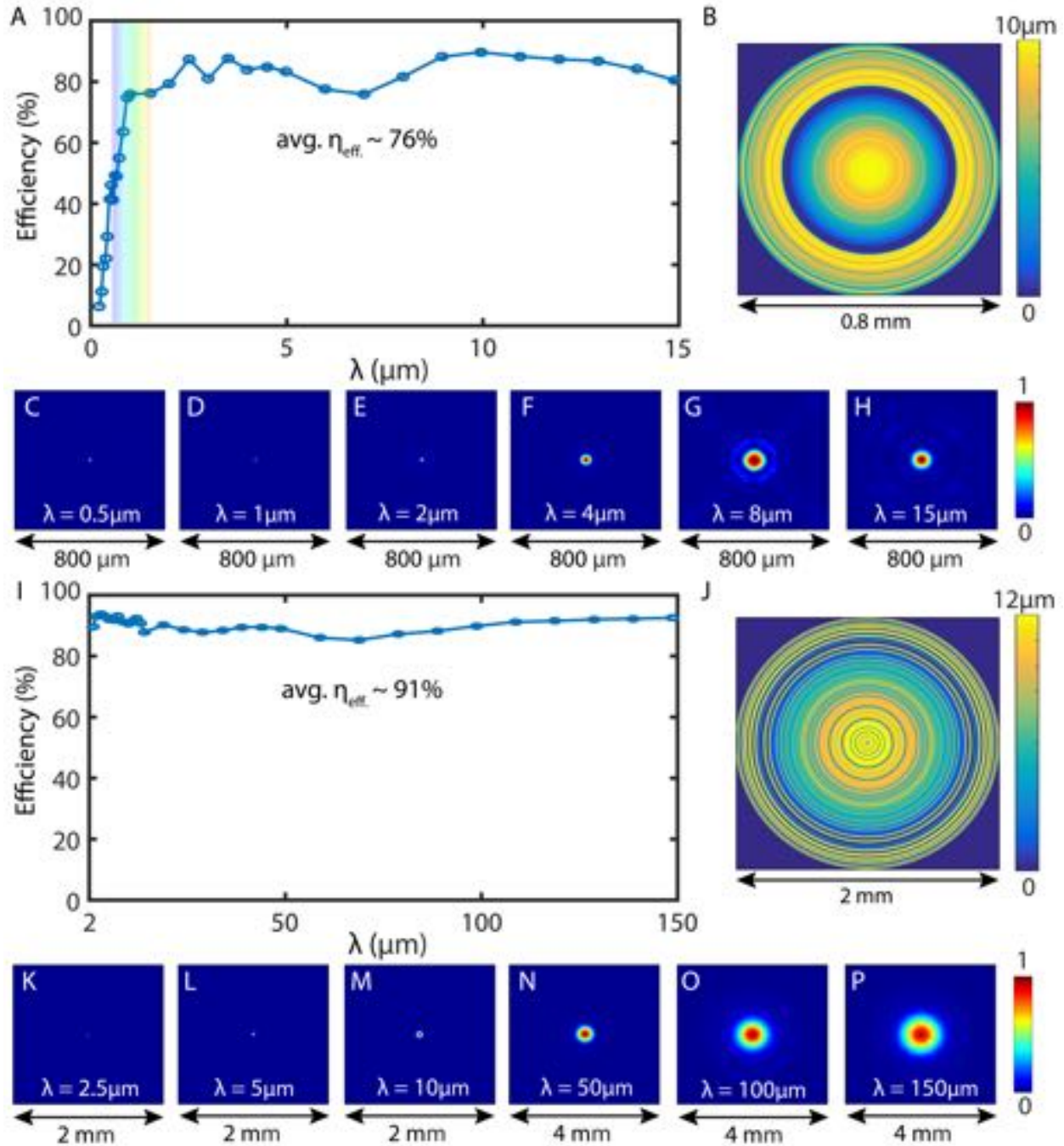


**Figure 5:** Achieving unlimited bandwidths. (A) Focusing-efficiency spectrum of an MDL with  $f=5\text{mm}$  and aperture  $=0.8\text{mm}$  for  $\lambda = 0.5\mu\text{m}$  to  $15\mu\text{m}$  assuming a photopolymer material. (B) Geometry of the MDL. The minimum feature width, maximum feature height and number of levels were  $6\mu\text{m}$ ,  $10\mu\text{m}$  and 100, respectively. (C-H) Simulated PSFs at exemplary wavelengths spanning the bandwidth. (I) Focusing-efficiency spectrum of an MDL with  $f=10\text{mm}$  and aperture of  $2\text{mm}$  for  $\lambda=2.5\mu\text{m}$  to  $150\mu\text{m}$  assuming Silicon as the MDL material. (J) MDL geometry. The minimum feature width, maximum feature height and number

*of levels were  $6\mu\text{m}$ ,  $12\mu\text{m}$  and 100, respectively. (K-P) Simulated PSFs at exemplary wavelengths spanning the bandwidth.*

We expect the performance of the lens to be directly related to the number of degrees of design freedom, which is the product of the number of rings in the radially symmetric lens and the number of height levels that can be occupied by each ring. We explored the impact of these degrees of freedom via simulations (Figs. S22 and S23) [16]. The average focusing efficiency of the MDL decreases with decreasing number of degrees of freedom as expected. However, the dependence seems to be relatively weak. Therefore, we attempted to design an MDL with an even larger operating bandwidth of  $\lambda=2.5\mu\text{m}$  to  $150\mu\text{m}$ . Note that we chose this bandwidth only because we were able to find the dispersion data for a transparent material (Silicon) for these wavelengths in literature (Fig. S3) [16]. The focusing efficiency of this MDL is shown as a function of wavelength in Fig. 5I. Note that the focusing efficiency is 91% averaged over  $\lambda=2.5\mu\text{m}$  to  $150\mu\text{m}$ . We remind the reader that this is achieved with a single diffractive surface! The height distribution of this MDL is shown in Fig. 5J. The minimum feature width, maximum feature height and number of levels were  $6\mu\text{m}$ ,  $12\mu\text{m}$  and 100, respectively. Exemplary simulated point-spread functions are shown in Figs. 5K-P (the corresponding plots for all the wavelengths are in Fig. S24 [16]). We also confirmed that the simulated FWHM closely tracks the diffraction limit (Fig. S25) [16]. Clearly, the MDL is achromatic over the entire wavelength range from  $2.5\mu\text{m}$  to  $150\mu\text{m}$ . In order to confirm that both MDLs will be useful for imaging, we simulated the wavefront aberrations as a function of wavelength and confirmed that the aberrations are indeed minimal across all the design wavelengths (Tables S5 and S6) [16]. We note again that we do not know the limit of this operating bandwidth. Our conjecture is that the bandwidth will be limited by the channel capacity theory dictated by Information Theory [26]. Nevertheless, allowing phase to be a free parameter seems to drastically reduce the constraints enabling a far larger operating bandwidth than we originally anticipated.

## **Conclusion**

We describe a generalized approach to lens design that allows the phase distribution in the image (or focal) plane to be a free parameter. This freedom allows the lens transmittance function to have numerous

solutions, and we propose that the choice of solution could be made to enable achromaticity, manufacturability, minimization of aberrations, of weight, of thickness, of cost, etc. We utilize this concept to design a single diffractive surface that is achromatic with a huge bandwidth (as large as 2.5 $\mu\text{m}$  to 150 $\mu\text{m}$ ) with no apparent practical limits. Our approach can be readily generalized to metasurfaces (by employing full-wave diffraction models), which could be advantageous to manipulate the polarization states of light [27] and could even be implemented in integrated-photonics platforms [28-30].

## Methods

### Design and Optimization

The multi-level diffractive lens (MDL) is modeled using scalar diffraction theory in the regime of Fresnel approximation. The beam propagation is modelled with the Fresnel-Kirchhoff diffraction integral as given in eqn. (1):

$$U(x', y', \lambda, d) = \frac{e^{ikd}}{i\lambda d} \iint g_{illum}(x', y', \lambda) \cdot T(x', y', \lambda) \cdot e^{i\frac{k}{2d}[(x-x')^2 + (y-y')^2]} dx \quad (1)$$

where  $T(x, y, \lambda)$  is the transmission function at the lens surface and  $g_{illum}(x', y', \lambda) = 1$  is the on-axis unit amplitude illumination wave. The intensity at the focal plane is given by  $I(x', y', \lambda, d) = |U(x', y', \lambda, d)|^2$ . We utilized a modified version of direct-binary search to optimize the height profile of rotationally symmetric MDLs consisting of individual constituent rings of width equal to a pre-defined value.

### FDTD Simulation

For the 0.5 $\mu\text{m}$  to 15 $\mu\text{m}$  broadband MDL design, an additional full wave 2D FDTD simulation was done to verify the achromaticity of the design as predicted from the scalar prediction. A full 3D simulation could not be pursued due to extreme computational requirement both in terms of memory and time complexity. Symmetry along the x-axis is exploited to reduce the simulation time by 1/2 of the original simulation requirements. Moreover, even with 2D FDTD simulation wavelengths smaller than 5 $\mu\text{m}$  is again

computationally expensive and has been avoided. Full details of the FDTD simulation setup has been provided in the supplementary information.

### **Fabrication and Characterization**

The achromatic diffractive lenses were patterned on a photoresist (S1813) film atop a glass wafer using grayscale laser patterning using a Heidelberg Instruments MicroPG101 tool. The exposure dose was varied as a function of position in order to achieve the multiple height levels dictated by the design. After fabrication, the devices were characterized on an optical bench by illuminating them with broadband collimated light, whose spectral bandwidth could be controlled by a tunable filter. The focus of the lenses were captured on a monochrome CMOS sensor for characterization of the PSF. Imaging performance of the lenses were tested in prototype cameras as described in the main text with various objects namely the Macbeth chart and USAF resolution chart.

### **Acknowledgements**

We thank Brian Baker, Steve Pritchett and Christian Bach for fabrication advice, and Tom Tiwald (Woollam) for measuring dispersion of materials. RM acknowledges useful discussion with Fernando Vasquez-Guevara. We would also like to acknowledge a grant of credit on Amazon AWS (051241749381) for computation. The support and resources from the Center for High Performance Computing at the University of Utah are also gratefully acknowledged. RM and BSR acknowledges funding from the Office of Naval Research grant N66001-10-1-4065 and from an NSF CAREER award: ECCS #1351389, respectively.

### **Competing Interests Statement**

RM is co-founder of Oblate Optics, Inc., which is commercializing technology discussed in this manuscript. The University of Utah has filed for patent protection for technology discussed in this manuscript.

### **Author Contributions**

RM, BSR and SB conceived and designed the experiments. SB and RM modeled and optimized the devices. MM fabricated the devices. SB and MM performed the PSF experiments. MM, SB and AM performed the imaging experiments. SB performed the MTF analysis. SB and AM performed the aberrations analysis. AM performed the distortion analysis. All authors performed the data analysis and wrote the manuscript.

### **Materials and Correspondence**

Correspondence and materials requests should be addressed to RM at [rmenon@eng.utah.edu](mailto:rmenon@eng.utah.edu).

## References

1. M. Born, and E. Wolf, *Principle of Optics*, 7th ed. (Cambridge University Press, Cambridge, **1999**).
2. P. Wang, and R. Menon, "Computational multi-spectral video imaging," *J. Opt. Soc. Am. A* **35**(1), 189-199 (2018).
3. R. Menon, P. Rogge, and H.-Y. Tsai, "Design of diffractive lenses that generate optical nulls without phase singularities," *J. Opt. Soc. Am. A*, **26**(2), 297 (2009).
4. S. R. R. Pavani, M. A. Thompson, J. S. Biteen, S. J. Lord, N. Liu, R. J. Tveit, R. Piestun and W. E. Moerner, "Three-dimensional, single-molecule fluorescence imaging beyond the diffraction limit by using a double-helix point-spread function," *PNAS* **106** (9) 2995-2999 (2009).
5. M. Khorasaninejad, W. T. Chen, A. Y. Zhu, J. Oh, R. C. Devlin, C. Roques-Carmes, I. Mishra and F. Capasso, "Visible wavelength planar metalenses based on titanium dioxide," *IEEE J. Selected topics of Quantum Electronics*, **23**(3) 4700216 (2017).
6. M. Meem, A. Majumder and R. Menon, "Multi-level micro-optics enables broadband, multi-plane computer-generated holography," [arXiv:1901.05943](https://arxiv.org/abs/1901.05943) [physics.optics]
7. N. Mohammad, M. Meem, X. Wan, and R. Menon, "Full-color, large area, transmissive holograms enabled by multi-level diffractive optics," *Sci. Rep.* **7**: 5789 | DOI: 10.1038/s41598-017-06229-5 (2017).
8. G. Kim, N. Nagarajan, E. Pastuzyn, K. Jenks, M. Capecchi, J. Sheperd and R. Menon, "Deep-brain imaging via epi-fluorescence computational cannula microscopy," *Sci. Rep.*, **7**:44791 DOI: 10.1038/srep44791 (2016).
9. G. Kim, N. Nagarajan, M. Capecchi and R. Menon, "Cannula-based computational fluorescence microscopy," *Appl. Phys. Lett.* **106**, 261111 (2015).
10. G. Kim and R. Menon, "Computational imaging enables a "see-through" lensless camera," *Opt. Exp.* **26**(18) 22826-22836 (2018)
11. G. Kim, K. Isaacson, R. Palmer and R. Menon, "Lensless photography with only an image sensor," *Appl. Opt.* **56**(23),6450-6456 (2017)



12. G. Kim, S. Kapetanovic, R. Palmer and R. Menon, "Lensless-camera based machine learning for image classification," *arXiv:1709.00408 [cs.CV] (open-access)*.
13. G. C. Sherman, "Integral-transform formulation of diffraction theory," *J. Opt. Soc. Am. A.* 57(12) 1490-1498 (1967).
14. P. J. Rogers, "Aberrations of optical systems," *Optics and Laser Technology*, 19(3) 161 (1987).
15. W.T. Chen, A.Y. Zhu, J. Sisler, Z. Bharwani, and F. Capasso, "A Broadband achromatic polarization-insensitive metalens consisting of anisotropic nanostructures." *Nat. Comm.* 10, 355 (2019).
16. Supplementary information online.
17. S. Banerji, M. Meem, A. Majumder, F.G. Vasquez, B. Sensale-Rodriguez and R. Menon, "Imaging with flat optics: metalenses or diffractive lenses?" *Optica* 6, 805 (2019).
18. P. Wang, N. Mohammad, and R. Menon, "Chromatic-aberration-corrected diffractive lenses for ultra-broadband focusing", *Sci. Rep.* 6, 21545 (2016).
19. N. Mohammad, M. Meem, B. Shen, P. Wang, and R. Menon, "Broadband imaging with one planar diffractive lens", *Sci. Rep.* 8 2799 (2018).
20. M. Meem, A. Majumder, and R. Menon, "Full-color video and still imaging using two flat lenses", *Opt. Exp.* 26(21) 26866-26871 (2018).
21. M. Meem, S. Banerji, A. Majumder, F. G. Vasquez, B. Sensale-Rodriguez, and R. Menon, Broadband lightweight flat lenses for longwave-infrared imaging. *arXiv: 1904.09011.* (2019)
22. S. Banerji and B. Sensale-Rodriguez, "A Computational Design Framework for Efficient, Fabrication Error-Tolerant, Planar THz Diffractive Optical Elements" *Sci. Rep.* 9, 5801 (2019).
23. S. Banerji, and B. Sensale-Rodriguez, "3D-printed diffractive terahertz optical elements through computational design." In *Micro-and Nanotechnology Sensors, Systems, and Applications XI* (Vol. 10982, p. 109822X). International Society for Optics and Photonics (2019).

24. A. Arbabi, Y Horie, A. J. Ball, M. Bagheri, and A. Faraon, "Subwavelength-thick lenses with high numerical apertures and large efficiency based on high-contrast transmitarrays." *Nat. Comm.* **6**, 7069 (2015).
25. R. Menon, P. Rogge, and H-Y. Tsai, "Design of diffractive lenses that generate optical nulls without phase singularities," *J. Opt. Soc. Am. A.* **26**(2), 297 (2009).
26. R. Shaw, "The application of Fourier techniques and information theory to the assessment of photographic image quality," *Photographic Science and Engineering*, 6(5), 281-286 (1962).
27. B. Shen, P. Wang, R. C. Polson and R. Menon, "An ultra-high efficiency Metamaterial Polarizer," *Optica* 1(5) 356-360 (2014).
28. B. Shen, P. Wang, R. C. Polson and R. Menon, "An integrated-nanophotonic polarization beamsplitter with  $2.4\mu\text{m} \times 2.4\mu\text{m}^2$  footprint," *Nat. Phot.*, 9, 378-382 (2015).
29. B. Shen, R. C. Polson and R. Menon, "Increasing the density of integrated-photonic circuits via nanophotonic cloaking," *Nat. Comms.* 7, 13126 (2016).
30. A. Majumder, B. Shen, R. C. Polson, and R. Menon, "Ultra-compact polarization rotation in integrated silicon photonics using digital metamaterials," *Opt. Express* 25, 19721-19731 (2017).

## Supplementary Information

# Imaging over an unlimited bandwidth with a single diffractive surface

*Sourangsu Banerji,<sup>1,\*</sup> Monjurul Meem,<sup>1,\*</sup> Apratim Majumder,<sup>1</sup> Berardi Sensale-Rodriguez<sup>1</sup> and Rajesh Menon<sup>1,2, a)</sup>*

<sup>1</sup>Department of Electrical and Computer Engineering, University of Utah, Salt Lake City, UT 84112, USA.

<sup>2</sup>Oblate Optics, Inc. San Diego CA 92130, USA.

a) [rmenon@eng.utah.edu](mailto:rmenon@eng.utah.edu)

\*Equal contribution.

### 1. Summary of the Literature survey of broadband achromatic metalenses

**Table S1.** Broadband Metalenses

Material	Wavelength	Bandwidth	N.A.	Focal Length/ Diameter	Simulated / Measured Efficiency	Feature Width/Height	Polarization	Reference
a-Si	1.3 $\mu$ m - 1.65 $\mu$ m	350 nm	0.24	200 $\mu$ m / 100 $\mu$ m	average 35% (measured)-	100 nm / 1400 nm	Polarization Insensitive	[1]
a-Si	1.2 $\mu$ m - 1.65 $\mu$ m	450 nm	0.13	800 $\mu$ m / 200 $\mu$ m	average 32% (measured)	100 nm / 800 nm	Polarization Insensitive	[1]
a-Si	1.2 $\mu$ m - 1.40 $\mu$ m	200 nm	0.88	30 $\mu$ m / 100 $\mu$ m	-	100 nm / 800 nm	Polarization Insensitive	[1]
GaN	400 nm - 660 nm	260 nm	0.106	235 $\mu$ m / 50 $\mu$ m	average 40% (measured)	45 nm / 800 nm	Circular	[2]
TiO <sub>2</sub>	460 nm - 700 nm	240 nm	0.2	67 $\mu$ m / 26.4 $\mu$ m	average 35% (measured)	50 nm / 600 nm	Polarization Insensitive	[11]
a-Si	1300 nm - 1800 nm	500 nm	0.04	7.5 mm / 600 $\mu$ m	24%, 22%, and 28%	75 nm / 600 nm	Linear	[3]
Au/SiO <sub>2</sub> /Au	1.2 $\mu$ m - 1.68 $\mu$ m	480 nm	0.268	100 $\mu$ m / 55.55 $\mu$ m	12.44 % (measured)	40nm / 30 nm	Circular	[4]

Au/SiO <sub>2</sub> /Au	1.2 nm - 1.68 μm	481 nm	0.217	-	8.4 % (measured)	40nm /30 nm	Circular	[4]
Au/SiO <sub>2</sub> /Au	1.2 nm - 1.68 μm	482 nm	0.324	-	8.56 % (measured)	40nm /30 nm	Circular	[4]
TiO <sub>2</sub>	470 nm - 670 nm	200	0.2	63 μm / 25.2 μm	50% (Simulated)	80 nm / 600 nm	Circular	[5]
PbTe	5.11 μm - 5.29 μm	180 nm	0.5 mm / -	-	-	/ 650 nm	-	[12]
GaSb	3 μm - 5 μm	2 μm	0.35	155 μm / >300 μm	70% (Simulated)	30 μm / 2 μm	Polarization Insensitive	[13]
a-Si	5 μm - 8 μm	3 μm	0.35	30*λ / -	-	- / 1.5*λ	Polarization Insensitive	[6]
a-Si	3.7 μm - 4.2 μm	0.5 μm	0.45	300 μm / 300 μm	~ 96% (Simulated)	/ 2 μm	Polarization Insensitive	[15]
GaN	435 nm - 685 nm	250 nm	0.17	20 μm / 7 μm	50% - 78% (Simulated)	160nm or 240 nm / 400 nm	Linear	[7]
Photoresist (polymer-ZEP520A)	436 nm - 685 nm	250 nm	0.17	20 μm / 7 μm	50% - 78% (Simulated)	160nm or 240 nm / 400 nm	Linear	[7]
PbTe	5.11 μm - 5.29 μm	180 nm	-	0.5 mm / 1 mm	~ 75% (Simulated)	2500 nm / 650 nm	Linear	[16]
Au	532 nm - 1080 nm	548 nm	-	7 μm / 10 μm	~ 20% (measured)	100 nm , 60 nm, 40 nm / 40 nm	Linear	[8]
a-Si	470 nm - 658 nm	188 nm	0.351	400 μm / 300 μm	Qualitative Agreement	- / 15 to 50 nm	Polarization Insensitive	[14]
TiO <sub>2</sub>	490 nm - 550 nm	60 nm	0.2	485 μm / 200 μm	Qualitative Agreement	varied / 180 nm	-	[9]
TiO <sub>2</sub>	560 nm - 800 nm	240 nm	upto 0.8	2 μm to 14 μm / 5.4 μm	> 50% (Simulated)	10 nm - 150 nm / 488 nm	Polarization Insensitive	[17]

fused Si	486 nm - 656 nm	170 nm	0.1	100 mm / 20 mm	-	1300 nm / 560 nm	Polarization Insensitive	[10]
----------	--------------------	--------	-----	-------------------	---	---------------------	-----------------------------	------

This discrepancy in the definition of focusing efficiency is observed across all the papers on metalens design. The definition of focusing efficiency in the highlighted broadband metalens papers above in Table S1 are summarized below:

**Reference 1:**

**Definition:**

To measure the focusing efficiency, the motor is first moved to the focal plane of the metalens and the iris is closed such that it corresponds to three to five times the FWHM of the focal spot. Then, the light is passed to the power meter. The ratio between the measured focused power and the incident power defines the focusing efficiency.

**Note:** The paper states, “the maximum shift from the mean focal length limited to 2–5% for the entire design bandwidth.” It is not clear from the paper whether the authors took 3 times or 5 time the FWHM of the focal spot.

**Reference 2:**

**Definition:**

The efficiency is defined as the ratio of the optical power of the focused circularly polarized beam to the optical power of the incident beam with opposite helicity.

**Reference 3:**

**Definition:**

Absolute efficiency is defined as the amount of power in the beam waist at the focal line, divided by the input power. The beam waist is the full width of the normalized intensity at  $1/e^2$  and is calculated by fitting the measured intensity distribution at the focal line to a Gaussian function. The input power is the amount of collimated power (beam diameter of 4 mm) that passes through an aperture with the same dimensions as the lens ( $600\text{-}\mu\text{m} \times 600\text{-}\mu\text{m}$ ).

**Reference 4:**

**Definition:**

The efficiency is defined as the ratio of light intensity from the focal spot at corresponding focal plane to the light intensity reflected by a metallic mirror with the same pixel sizes. (For circularly polarized incidences in a reflection scheme)

**Reference 8:**

**Definition:**

The transmission efficiency is defined as the ratio of power transmitted through the lattice over the incident intensity. The diffraction efficiency, or the power focused within the focal point, was between 1.5% and 6%.

**Reference 11:**

**Definition:**

The achromatic metalens was also characterized by measuring the focusing efficiency of the focal spot under different polarizations of incident light. The focusing efficiency is defined as the focal spot power divided by transmitted power through an aperture with the same diameter as the metalens. The measured focusing efficiencies weakly change with polarization.

**Note:** The paper states “The metalens exhibits a measured focal length shift of only 9%  $\lambda = 460\text{--}700\text{ nm}$  and has diffraction-limited focal spots across the entire range. The focusing efficiency of the metalens varies by only  $\sim 4\%$  under various incident polarizations.”

## 2. Material dispersion

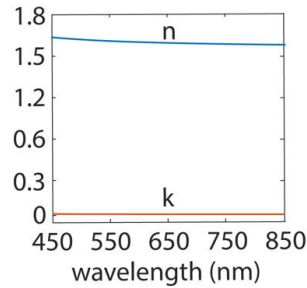


**Fig. S1:** Dispersion of Si813. This is used for the lens in Figs. 1-4.

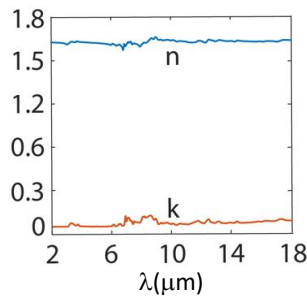


**Fig. S2:** Dispersion of AZ9260. This is used for the lens in Figs. 5A-H.

**Note:** A value of  $n = 1.61$  and  $k = 0$  was assumed for all wavelengths below  $2\ \mu\text{m}$  (typically the visible band) during optimization.

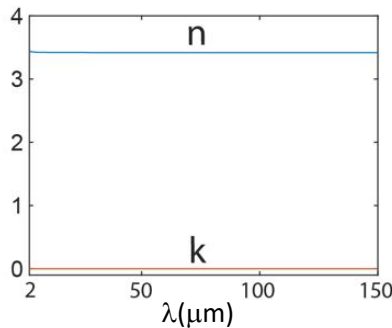


**Fig. S3:** Dispersion of silicon [26,27]. This is used for the lens in Figs. 5I-P.

## 3. Simulated and Measured Point Spread Functions (PSFs) of the 450nm – 850nm broadband MDL

The scalar simulated point spread functions (PSFs) for the broadband lens designed are provided below:

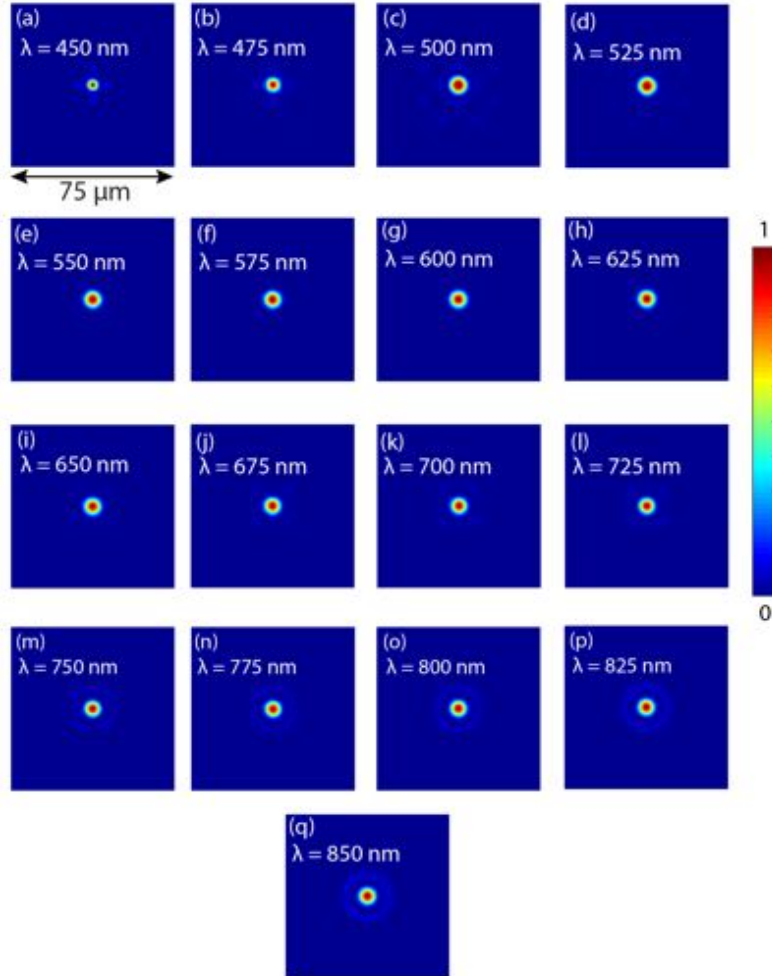


**Fig. S4:** Simulated PSFs for (a) 450nm (b) 475 nm (c) 500 nm (d) 525 nm (e) 550 nm (f) 575 nm (g) 600 nm (h) 625 nm (i) 650 nm (j) 675 nm (k) 700 nm (l) 725 nm (m) 750 nm (n) 775 nm (o) 800 nm (p) 825 nm and (q) 850 nm.

The measured point spread functions (PSFs) for the broadband lens designed are provided below:

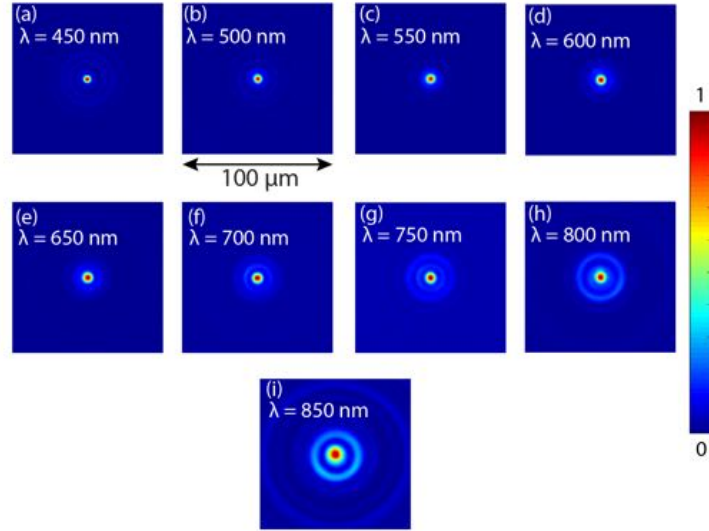


**Fig. S5:** Measured PSFs for (a) 450nm (b) 500 nm (c) 550 nm (d) 600 nm (e) 650 nm (f) 700 nm (g) 750 nm (h) 800 nm and (i) 850 nm.

#### 4. Fabrication

The achromatic MDL depicted was patterned in a photoresist (Microchem, S1813) film atop a glass wafer (thickness  $\sim 0.6$  mm) using grayscale laser patterning with a Heidelberg Instruments MicroPG101 tool [18-20]. In such conventional gray-scale lithography, the write head scans through the sample surface and the exposure dose at each point is modulated with different gray-scales [18, 19] (see schematic illustration of Fig. S4). Most of these typical photoresists are characterized by a contrast curve. Different depths in accord with different exposure doses are achieved after development. Greater dose leads to deeper feature. Before patterning structures, it is needed to calibrate this contrast curve. In this case, too, the exposure dose was varied with respect to position to achieve the multiple height levels dictated by the design.

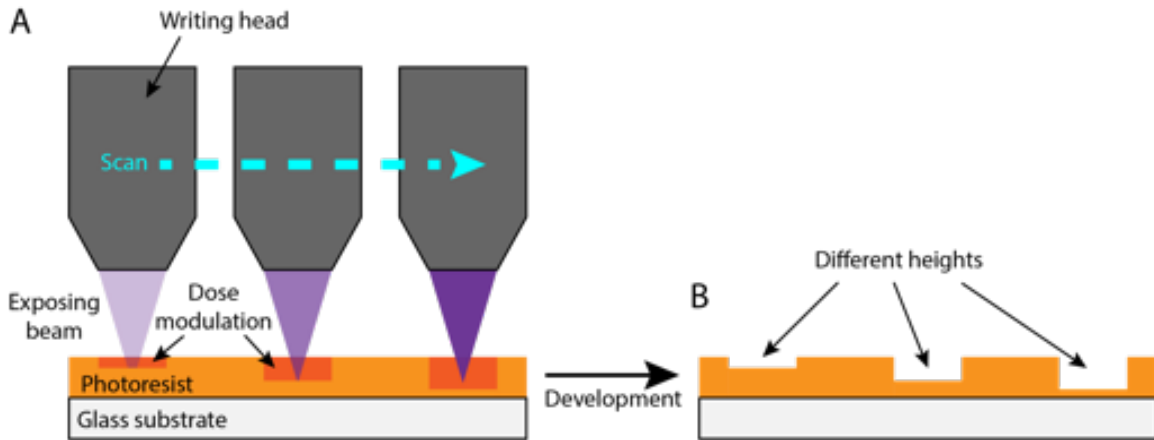


**Fig. S6:** Schematic of grayscale lithography used for fabricating the MDLs.

#### 5. Experiment details

##### 5.1. Focal spot characterization

The flat lenses were illuminated with expanded and collimated beam from a SuperK EXTREME EXW-6 source (NKT Photonics) and the SuperK VARIA filter (NKT Photonics). The wavelength and bandwidth can be changed using the VARIA filter. The focal planes of the flat lenses were



magnified using an objective (RMS20X-PF, Thorlabs) and tube lens (ITL200, Thorlabs) and imaged onto monochrome sensor (DMM 27UP031-ML, Imaging Source). The gap between objective and tube lens was  $\sim 90$  mm and that between the sensor and the backside of tube lens was about 148mm. The magnification of the objective-tube lens was 22.22X.

After capturing the focal spot, the Focusing efficiency was then calculated using the following equation: Focusing efficiency = (sum of pixel values in  $3 \times \text{FWHM}$ ) / (sum of pixel values in the entire lens area)

## 5.2. Image characterization

For resolution chart imaging, the 1951 USAF resolution test chart (R3L3S1N, Thorlabs) was used as the object. The flat lenses were used for imaging the object on to the sensor. A diffuser was placed behind the USAF target. The experimental setup is shown in Fig. S7. The USAF target was illuminated with the design wavelengths with 10nm bandwidth and corresponding images were captured using a monochrome sensor (DMM 27UP031-ML, Imaging Source). The exposure time was adjusted to ensure that the images did not get saturated. In each case, a dark frame was recorded and subtracted from the USAF target images.

For imaging colorful objects, the objects were placed in front of the MDL just like the resolution chart. But this time the objects were illuminated with white LED light instead of a laser and corresponding images were captured using a color sensor (DFM 72BUC02-ML, Imaging Source).

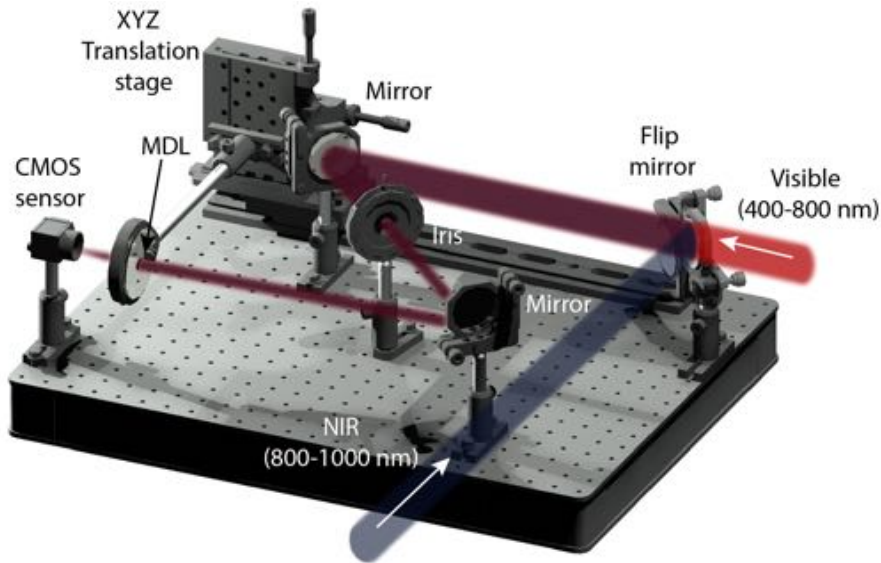


*Fig. S7: Schematic of system used for focusing experiments.*

The following supplementary videos are also included:

- Supplementary Video 1 shows a Macbeth color chart being moved around under visible light (450nm to 750nm).
- Supplementary Video 1 shows a Macbeth color chart being moved around under near-IR light (800nm to 850nm).

## 5.3. Simulated fabrication error analysis

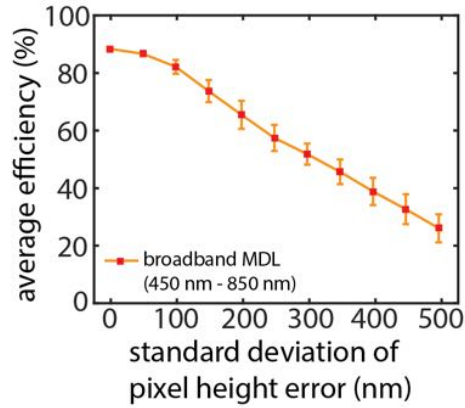


**Fig. S8:** Standard deviation based random pixel-height error analysis for the MDL designs.

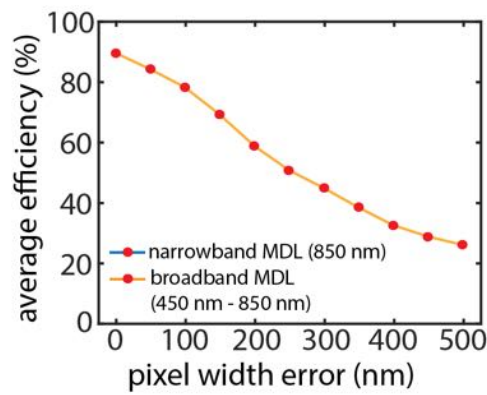


**Fig. S9:** pixel-width error analysis for the MDL designs

We measured the pixel width of 20 randomly selected zones and these are summarized in Fig. S10 along with the corresponding design zone width. The estimated error has a mean of 270nm and standard deviation of 166nm.

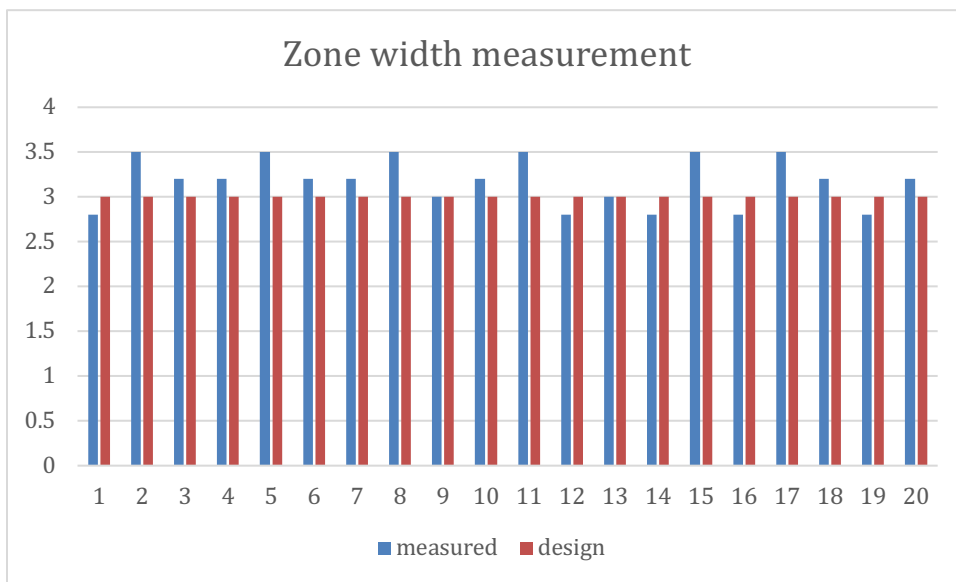


**Fig. S10:** Measured and design zone width of 20 randomly selected zones.

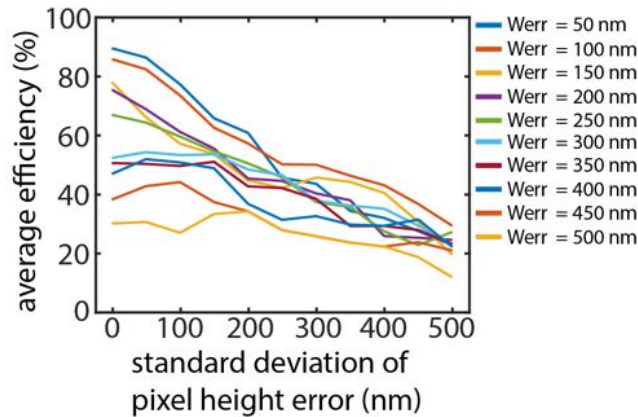


**Fig. S11:** Pixel-width + standard deviation based pixel-height error analysis for the broadband MDL design (Werr denotes error in pixel-width)

#### 5.4. Resolution from the USAF 1951 chart

Resolution test targets are typically used to measure the resolution of an imaging system. They consist of reference line patterns with well-defined thicknesses and spacing, which being designed to be kept in the same plane as the object being imaged. By identifying the largest set of non-distinguishable lines, one determines the resolving power of a given system. The R3L3S1N from Thorlabs (as used here) negative target uses chrome coating to cover the substrate, leaving the pattern itself clear, and works well in back-lit and highly illuminated applications.

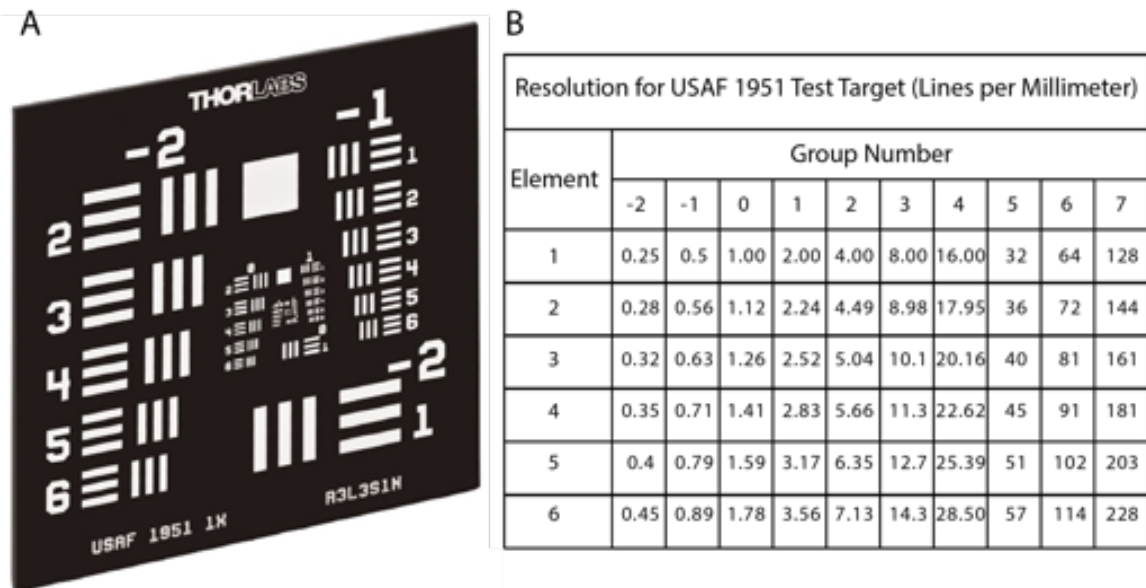


**Fig. S12:** A. Resolution Target Chart USAF 1951 B. Resolution Characterization chart for the resolution target.

Because these targets feature sets of three lines, they reduce the occurrence of spurious resolution and thus help prevent inaccurate resolution measurements.

### 5.5. Resolution chart images for different illumination wavelengths of the 450nm – 850nm broadband MDL

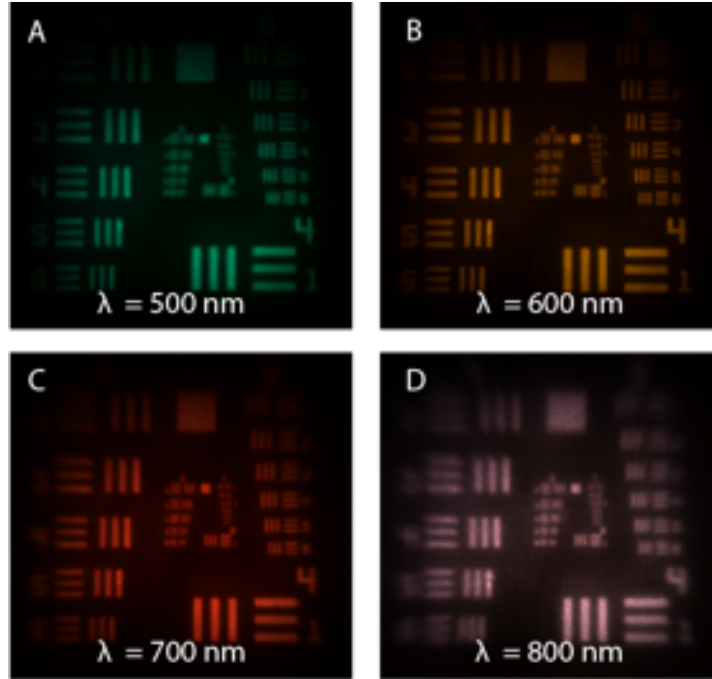


**Fig. S13:** Resolution chart image for the illumination wavelength **A.** 500nm **B.** 600nm **C.** 700nm and **D.** 800nm. The bandwidth at each wavelength was 100nm.

### 6. Aberrations analysis for measured wavefront of broadband (450 nm – 850 nm) MDL

The following optical setup, shown in Figs. S14A and B was constructed to measure the aberrations of the VIS/NIR MDL using a Shack Hartmann wavefront sensor. The incident (at wavelengths 450-850 nm) beam from a SuperK EXTREME EXW-6 source [21], connected to a SuperK VARIA filter [22] was expanded and collimated and directed using a series of optical mirrors toward the measurement setup. An iris was placed in the path of the beam to limit the beam diameter. The final beam was set to have a diameter of 25.4 mm. This beam was incident on the MDL. A Shack-Hartmann wavefront sensor from Thorlabs (WFS 150-7AR) was placed 7.7 mm (MDL to outer rim of the wavefront sensor) behind the test lens [23, 24]. The distance between the outer rim to the sensor plane is 13.6 mm, making the total distance between the MDL being tested and the wavefront sensor to be 21.3 mm. The incoming collimated beam converges to a focal spot at  $\sim 1$  mm behind the MDL and then diverges, before contacting the wavefront sensor. Hence, it is expected that the sensor should show a diverging wavefront. We selected 2.3 mm as the diameter of the pupil of the Shack Hartmann wavefront sensor (SH WFS). This ensures that neither is the beam clipped, nor oversampled. Similar experiment was performed with a stock refractive singlet lens as shown in Fig. S14A and the aberrations of the stock lens compared with those corresponding to our MDL.

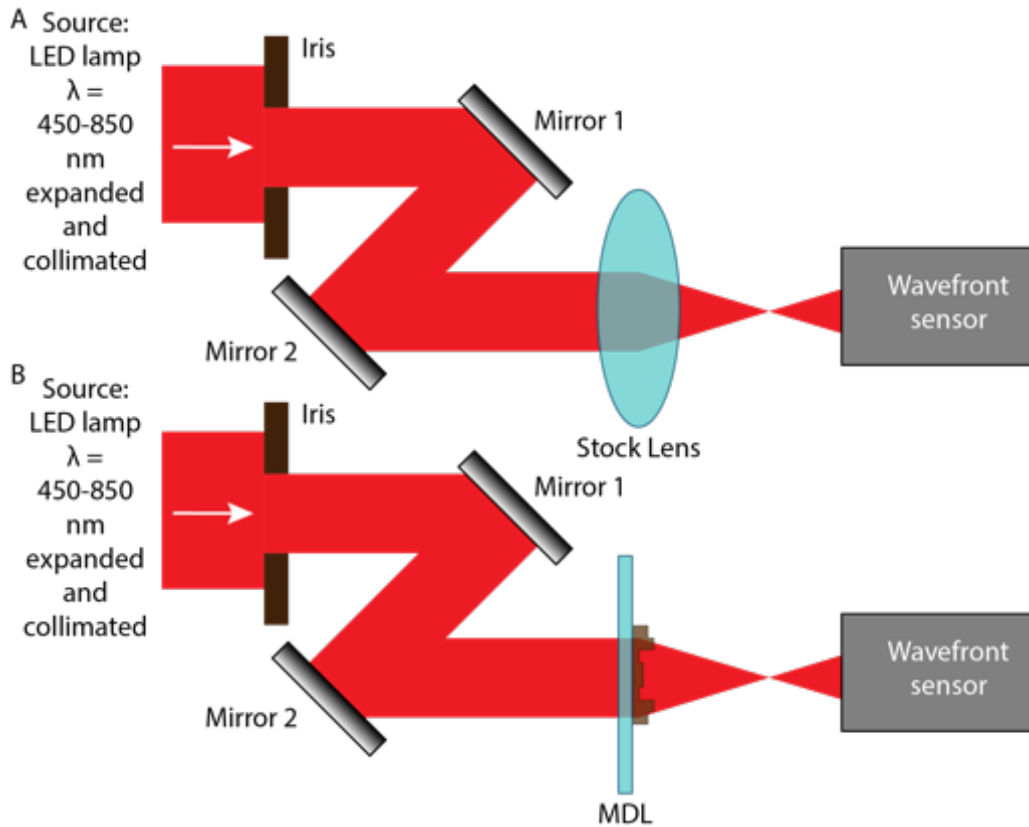


**Fig. S14:** Optical setup used to measure aberrations of a test VIS/NIR multi-level diffractive lens. The wavefront sensor is illuminated by a diverging wavefront produced after a collimated beam is brought into focus  $\sim 1\text{mm}$  behind the MDL. A series of mirrors, iris and lens are used to relay the beam from the source to the MDL. Setup for testing a (A) stock refractive singlet lens and (B) our MDL.

First, we used a stock refractive singlet lens (plano-convex lens, Thorlabs) to test and calibrate the setup. The measurements from this are shown in Fig. S15. The alignment is confirmed to be good from the results obtained. Focal length of the lens as obtained from the SH WFS is checked with the know focal length. The known focal length of the lens was 200 mm as specified by the manufacturer. We measured the focal length to be 200.86 mm under the broadband illumination (450-850 nm) and 200.86 mm under 600 nm illumination based on the data gathered from the SH WFS. This step serves as a calibration step and the values of the stock lens serve as ground truth. Later, we compared the aberration values obtained for the MDL against this stock lens. Next, the MDL was placed in the location of the stock lens and the measurement was repeated. The measured focal lengths of the MDL were 0.988 mm under the broadband illumination (450-850 nm) and 1.06 mm under 600 nm illumination based on the data gathered from the SH WFS. The wavefronts for the stock lens and the MDL under various illumination conditions are presented in Fig. S15.

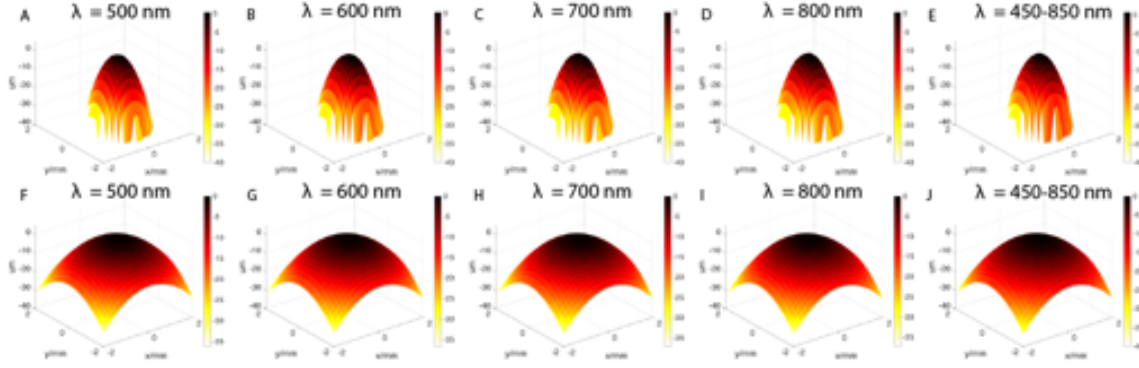


**Fig. S15:** Wavefronts for (A-E) for the MDL and (F-J) for the stock refractive singlet lens under (A-D and F-I) narrowband illuminations at 500, 600, 700 and 800 nm with 50 nm bandwidth and (E and J) broadband illumination at 450-850 nm. The wavefronts of the stock lens were used as ground truth and for system calibration.

**Table S2.** Measured aberration values for the test MDL lens and the stock refractive singlet lens

Aberration	Test MDL Value ( $\mu\text{m}$ )					Stock refractive singlet lens Value ( $\mu\text{m}$ )				
	$\lambda = 500$ nm	$\lambda = 600$ nm	$\lambda = 700$ nm	$\lambda = 800$ nm	$\lambda = 450$ - 850 nm	$\lambda = 500$ nm	$\lambda = 600$ nm	$\lambda = 700$ nm	$\lambda = 800$ nm	$\lambda = 450$ - 850 nm
Piston	7.039	6.904	7.077	6.969	4.981	5.678	5.784	5.762	5.802	5.777
Tip Y	1.467	1.503	0.508	0.595	2.822	-	-0.605	-0.561	-0.582	-0.62
Tilt X	0.199	0.234	0.945	0.877	0.831	0.438	0.433	0.471	0.478	0.471
Astigmatism $\pm 45^\circ$	0.013	0.003	0.02	0.011	0.008	0.02	0.022	0.022	0.021	0.019
Defocus	-8.684	-8.537	-8.565	-8.495	-8.592	-	-5.708	-5.771	-5.797	-5.72
Astigmatism $0/90^\circ$	0.008	0.009	0.008	0.029	-0.009	0.072	0.074	0.078	0.081	0.076
Trefoil Y	0.001	0.004	-0.028	-0.009	0.001	-	-0.003	-0.002	-0.003	-0.001
Coma X	-0.008	-0.022	0.016	0.007	0.007	-	-0.007	-0.009	-0.007	-0.008
Coma Y	-0.014	-0.009	0.008	0.006	0.004	0.008	0.01	0.011	0.009	0.008
Trefoil X	0.005	0.009	-0.009	-0.002	-0.001	-	-0.002	-0.003	-0.004	-0.005
Tetrafoil Y	0.007	0.001	0.001	0.005	0	-	-0.003	-0.003	-0.002	-0.003
Sec. Astig. Y	-0.002	0.003	-0.005	0	0.002	0.001	0.002	0.001	0.001	0.001
Spher. Aberr. $3^{\text{rd}}$ O	-0.016	-0.111	0.032	-0.018	-0.053	0.002	0.002	0.004	0.003	0.004
Sec. Astig. X	-0.003	-0.003	-0.003	-0.003	0.004	0.001	0	0	0	0
Tetrafoil X	-0.013	0.013	-0.006	0.027	-0.006	0	-0.001	0.001	0	0.001

## 7. Aberrations analysis for simulated wavefront

The Zernike polynomial coefficient were fitted over a circular shaped pupil. The calculation was done using the reference. The fit was using the least squares fit method. Fringe indexing scheme was used.

**Table S3: Aberrations coefficients**

Radial degree (n)	Azimuthal degree (m)	Fringe index (j)	Classical name
0	0	1	piston
1	1	2	tip
1	-1	3	tilt
2	0	4	defocus
2	2	5	vertical astigmatism
2	-2	6	oblique astigmatism
3	1	7	horizontal coma
3	-1	8	vertical coma
4	0	9	primary spherical
3	3	10	oblique trefoil
3	-3	11	vertical trefoil
4	2	12	vertical secondary astigmatism
4	-2	13	oblique secondary astigmatism
4	4	14	vertical quadrafoil
4	-4	15	oblique quadrafoil

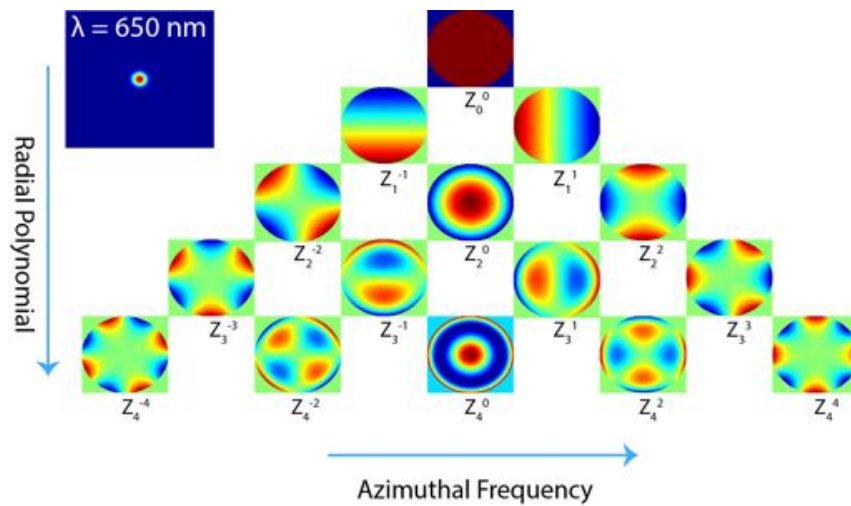


**Fig. S16:** Simulated wavefront analysis using Zernike coefficients for broadband MDL at  $\lambda = 650$  nm

**Table S4:** Broadband (450 nm – 850 nm) MDL with NA = 0.075, f = 1 mm

Wave lengt	Piston	Ti p	Til t	Defocu s	Verti cal astig	Obliq ue astig	Hori zont al	Verti cal	Prima ry	Obl iqu e	Ver tica l	Verti cal secon	Obliq ue secon	Vert ical quad	Obli que quad
---------------	--------	---------	----------	-------------	-----------------------	----------------------	--------------------	--------------	-------------	-----------------	------------------	-----------------------	----------------------	----------------------	---------------------

h (nm)					matis m	matis m	com a	co ma	spheri cal	tref oil	tref oil	dary astig matis m	dary astig matis m	rafoi l	rafoi l
450	1.89E-04	-2.7E-07	-2.7E-07	-0.0005284113	1.69E-11	-1.10E-09	1.09E-06	1.09E-06	0.00076652743	6.89E-10	-6.89E-10	8.37E-11	5.42E-09	4.51E-07	-8.94E-16
475	0.00028775822	-3.1E-07	-3.1E-07	-0.00080884405	9.52E-12	-1.26E-09	1.23E-06	1.23E-06	0.0011895377	3.13E-09	-3.12E-09	6.56E-11	6.05E-09	8.37E-07	1.79E-14
500	0.00044647048	-3.6E-07	-3.6E-07	-0.001252948	8.76E-12	-1.44E-09	1.45E-06	1.45E-06	0.0018368324	3.90E-09	-3.90E-09	2.82E-11	7.22E-09	1.49E-06	4.66E-14
525	0.00043882147	-2.9E-07	-2.9E-07	-0.0012238218	3.86E-12	-1.17E-09	1.26E-06	1.26E-06	0.0017717417	1.26E-09	-1.26E-09	1.42E-11	6.45E-09	1.87E-06	-6.06E-14
550	0.00036772378	-2.3E-07	-2.3E-07	-0.0010180837	4.78E-12	-9.42E-10	1.09E-06	1.09E-06	0.0014532738	-4.40E-10	4.40E-10	1.44E-11	5.68E-09	2.14E-06	3.31E-14
575	0.00033477173	-2.2E-07	-2.2E-07	-0.00092151144	4.42E-12	-8.88E-10	1.08E-06	1.08E-06	0.0013021866	1.42E-09	-1.42E-09	3.61E-12	5.68E-09	2.63E-06	1.99E-14
600	0.00032281689	-2.1E-07	-2.1E-07	-0.00088604301	8.08E-12	-8.58E-10	1.12E-06	1.12E-06	0.0012478773	1.42E-08	-1.42E-08	-1.10E-11	5.93E-09	3.22E-06	1.17E-14
625	0.00030532011	-2.1E-07	-2.1E-07	-0.00083823217	7.81E-13	-7.92E-10	1.08E-06	1.08E-06	0.0011845863	2.15E-08	-2.15E-08	-8.23E-12	5.76E-09	3.59E-06	8.18E-14
650	0.00027390639	-1.9E-08	-1.9E-08	-0.00075407029	-6.17E-12	-8.23E-10	9.16E-07	9.16E-07	0.0010747632	-4.60E-09	4.60E-09	1.32E-11	4.76E-09	3.61E-06	1.97E-14



		-07	-07												
675	0.00023984583	1.63E-07	1.63E-07	0.00066312635	2.78E-12	6.26E-10	7.46E-07	7.47E-07	0.00095563574	1.98E-09	1.98E-09	1.87E-12	3.92E-09	3.42E-06	2.67E-14
700	0.00021409358	1.34E-07	1.34E-07	0.00059477816	4.90E-12	5.34E-10	5.97E-07	5.97E-07	0.0008669591	3.83E-09	3.83E-09	2.94E-11	3.06E-09	3.22E-06	1.12E-14
725	0.00019938	1.12E-07	1.12E-07	0.00055640505	2.45E-12	4.39E-10	4.90E-07	4.90E-07	0.00081926677	6.39E-09	6.39E-09	4.37E-12	2.50E-09	3.12E-06	1.01E-14
750	0.00019441386	1.02E-07	1.02E-07	0.00054452999	4.93E-12	3.92E-10	4.12E-07	4.12E-07	0.00080814079	7.56E-10	7.56E-10	5.76E-12	2.10E-09	3.15E-06	8.09E-14
775	0.00019743654	9.20E-08	9.20E-08	0.000554355608	5.41E-12	3.74E-10	3.75E-07	3.75E-07	0.00082709669	6.37E-09	6.37E-09	7.95E-12	1.86E-09	3.33E-06	1.59E-14
800	0.00020730276	9.00E-08	9.00E-08	0.0005827109	7.27E-14	3.41E-10	3.59E-07	3.59E-07	0.00087170815	5.87E-09	5.87E-09	2.29E-12	1.82E-09	3.65E-06	6.94E-15
825	0.00022363955	9.39E-08	9.38E-08	0.00062846224	2.60E-12	3.51E-10	3.66E-07	3.66E-07	0.00094021123	3.32E-09	3.32E-09	1.11E-11	1.88E-09	4.16E-06	2.08E-14
850	0.00024661465	1.04E-07	1.04E-07	0.0006918846	4.00E-12	4.63E-10	4.00E-07	4.00E-07	0.0010326691	1.44E-09	1.44E-09	1.16E-11	1.96E-09	4.86E-06	3.61E-14

**Table S5:** Broadband (0.5 $\mu$ m –15 $\mu$ m) MDL with NA = 0.0797, f = 5 mm

Wavelength	Piston	Tilt	Tilt	Defocus	Vertical astig	Oblique astig	Horizontal	Vertical	Primary	Oblique	Vertical	Vertical second	Oblique second	Vertical	Oblique
------------	--------	------	------	---------	----------------	---------------	------------	----------	---------	---------	----------	-----------------	----------------	----------	---------

th (um)					matism	matism	coma	coma	spherical	trefoil	trefoil	daryastigmatism	daryastigmatism	quadrifoil	drafoil
0.2	0.043129627	5.33E-05	5.33E-05	-0.00051947299	1.54E-08	1.24E-07	-2.33E-05	-2.33E-05	0.0015698343	-1.30E-04	1.30E-04	3.70E-09	2.54E-06	0.004240674	-1.75E-10
0.25	0.050028447	-1.70E-05	-1.70E-05	-0.0052477336	8.97E-09	2.96E-06	-9.29E-05	-9.29E-05	0.011984387	-7.17E-05	7.17E-05	-8.55E-09	4.65E-06	1.84E-02	-9.36E-10
0.3	0.022603258	-1.74E-05	-1.74E-05	0.0084305527	1.74E-09	-1.12E-06	-1.19E-05	-1.19E-05	0.0028690433	-2.83E-05	2.83E-05	-7.08E-09	-2.39E-06	0.005442712	3.40E-10
0.35	0.024987604	-1.90E-05	-1.90E-05	-0.014578459	-2.58E-10	4.33E-07	4.90E-06	4.89E-06	5.90E-05	-3.90E-05	3.90E-05	-4.99E-09	6.50E-07	-6.77E-03	-1.47E-10
0.4	0.012688935	-2.59E-05	-2.59E-05	-0.00094959908	4.62E-09	-4.52E-07	9.49E-06	9.48E-06	-0.00089047517	-6.20E-06	6.20E-06	-2.64E-10	-6.35E-07	-1.20E-03	-3.81E-10
0.45	0.0058505274	-1.10E-05	-1.10E-05	0.00042408373	-1.55E-09	-7.16E-06	-2.46E-05	-2.46E-05	0.00069258973	2.07E-05	-2.07E-05	2.22E-11	-1.21E-05	3.84E-04	5.60E-11
0.5	0.004202839	-7.22E-06	-7.22E-06	0.0015095581	-6.70E-10	-6.09E-07	-1.58E-05	-1.58E-05	0.001563885	-3.59E-06	3.59E-06	2.29E-10	-1.04E-06	3.55E-03	-4.48E-11
0.55	0.0027676001	-2.54E-06	-2.54E-06	0.0012221405	-1.37E-09	-1.92E-07	2.87E-06	2.87E-06	0.00094057049	1.55E-05	-1.55E-05	2.47E-10	-3.60E-07	3.38E-03	3.27E-11
0.6	0.0037813571	6.31E-06	6.31E-06	0.0019563679	6.30E-10	-5.14E-07	5.24E-06	5.24E-06	0.0025530409	2.00E-05	-2.00E-05	-1.23E-09	-7.95E-07	5.67E-03	-1.43E-11

0.7	0.0014 83194 5	8.7 7E - 07	8.7 5E - 07	- 0.0004 39508 09	6.74E -10	- 6.27E -08	4.35 E-06	4.3 6E- 06	0.0015 09659 7	- 9.5 0E- 07	9.4 8E- 07	6.39E -11	- 9.06E -08	3.16E- 03	- 8.51 E-12
0.8	0.0006 28568 46	- 2.5 2E - 07	- 2.5 1E - 07	- 0.0009 53899 93	1.39E -10	1.04E -08	3.84 E-06	3.8 4E- 06	0.0011 56916 7	- 4.9 4E- 07	4.9 4E- 07	- 1.03E -10	4.28E -08	6.17E- 04	1.12 E-12
0.9	0.0003 21576 78	- 1.1 4E - 08	- 1.1 2E - 08	- 0.0007 80975 85	5.17E -12	1.28E -09	3.43 E-07	3.4 2E- 07	0.0008 97051 53	1.2 3E- 07	- 1.2 3E- 07	- 4.88E -11	- 2.72E -09	1.35E- 05	- 2.17 E-13
1	0.0002 29173 53	- 2.2 9E - 07	- 2.2 9E - 07	- 0.0005 59896 35	5.84E -12	- 8.05E -10	9.06 E-07	9.0 5E- 07	0.0006 09256 44	- 3.2 3E- 09	3.2 4E- 09	2.94E -11	4.07E -09	- 3.61E- 06	- 9.59 E-14
1.1	0.0001 95770 34	- 2.3 3E - 07	- 2.3 3E - 07	- 0.0004 70798 52	9.81E -12	- 8.00E -10	7.24 E-07	7.2 4E- 07	0.0004 99498 45	- 8.0 7E- 08	8.0 7E- 08	- 4.62E -11	2.35E -09	- 2.95E- 06	9.77 E-14
1.5	0.0004 38045 04	- 4.1 9E - 07	- 4.1 9E - 07	- 0.0010 46839 2	- 1.06E -11	- 1.68E -09	1.39 E-06	1.3 9E- 06	0.0011 44875 5	- 2.0 0E- 07	2.0 0E- 07	9.53E -11	6.19E -09	- 4.14E- 06	- 1.78 E-13
2	0.0003 52110 8	2.2 4E - 07	2.2 4E - 07	- 0.0008 59518 24	6.14E -12	2.11E -09	- 3.33 E-07	- 3.3 3E- 07	0.0010 70572 4	1.7 4E- 07	- 1.7 4E- 07	- 4.18E -11	- 7.64E -09	- 1.23E- 06	- 9.90 E-14
2.5	0.0004 17029 86	- 8.3 3E - 08	- 8.3 4E - 08	- 0.0009 47792 14	2.09E -11	1.90E -10	1.60 E-06	1.6 0E- 06	0.0011 12667 4	2.6 9E- 07	- 2.6 9E- 07	- 4.93E -11	5.94E -09	7.76E- 06	- 2.25 E-13
3	0.0010 58187 9	- 4.0 1E - 06	- 4.0 1E - 06	- 0.0023 17015 5	1.20E -10	- 2.01E -08	1.40 E-05	1.4 0E- 05	0.0024 88706 3	- 4.1 5E- 07	4.1 5E- 07	- 8.33E -11	4.52E -08	- 3.97E- 06	- 6.56 E-13
3.5	0.0008 16078 45	- 1.6 3E - 06	- 1.6 3E - 06	- 0.0017 12887 2	- 3.22E -11	2.44E -09	5.53 E-06	5.5 3E- 06	0.0018 22583 6	- 3.3 7E- 07	3.3 7E- 07	- 1.88E -10	3.25E -08	1.84E- 05	1.19 E-12

4	0.0016 43423 3	- 1.6 4E - 06	- 1.6 4E - 06	- 0.0033 41037 3	- 1.38E -11	- 2.77E -08	4.84 E-06	4.8 4E- 06	0.0035 24535 1	- 1.5 5E- 06	1.5 5E- 06	- 1.45E -10	- 3.21E -08	- 1.04E- 05	- 1.24 E-12
4.5	0.0017 36434 4	- 8.6 7E - 08	- 8.6 2E - 08	- 0.0036 12043 6	- 1.28E -11	1.00E -08	- 4.49 E-07	- 4.4 8E- 07	0.0040 64277 3	- 1.3 2E- 06	1.3 2E- 06	4.64E -10	- 3.08E -08	- 6.82E- 05	4.52 E-12
5	0.0019 42146 3	1.3 7E - 06	1.3 7E - 06	- 0.0041 69199 6	- 6.33E -11	1.15E -08	- 6.40 E-06	- 6.4 0E- 06	0.0051 36448	1.0 3E- 06	1.0 3E- 06	- 4.05E -11	- 1.01E -07	- 7.44E- 05	1.99 E-13
6	0.0027 85100 1	4.4 5E - 06	4.4 5E - 06	- 0.0065 79860 1	- 6.52E -11	- 3.62E -09	- 1.32 E-05	- 1.3 2E- 05	0.0089 31388 1	4.8 5E- 06	- 4.8 5E- 06	2.48E -10	- 2.60E -07	- 1.03E- 04	- 1.68 E-12
7	0.0053 72375 7	3.8 0E - 06	3.8 0E - 06	- 0.0128 21789	- 1.19E -10	6.11E -08	- 7.31 E-06	- 7.3 2E- 06	0.0168 66619	7.8 4E- 06	- 7.8 4E- 06	- 5.67E -10	- 3.72E -07	- 0.0002 34516 03	- 4.49 E-12
8	0.0048 78306 3	- 2.2 1E - 06	- 2.2 1E - 06	- 0.0115 65058	- 1.46E -10	4.53E -08	2.17 E-06	2.1 7E- 06	0.0148 58129	3.5 6E- 06	- 3.5 6E- 06	- 1.52E -10	- 3.14E -07	- 1.15E- 04	- 1.22 E-12
9	0.0026 42727	2.2 8E - 06	2.2 8E - 06	- 0.0064 54710 4	- 1.59E -10	3.15E -08	- 1.16 E-05	- 1.1 6E- 05	0.0088 61100 3	9.6 6E- 07	- 9.6 6E- 07	- 1.99E -10	- 1.73E -07	- 7.49E- 05	1.48 E-12
10	0.0024 06370 8	3.5 2E - 06	3.5 2E - 06	- 0.0058 75878 5	- 5.27E -11	4.22E -08	- 1.29 E-05	- 1.2 9E- 05	0.0081 24131 7	2.1 7E- 06	- 2.1 7E- 06	1.09E -11	- 1.52E -07	- 7.83E- 05	- 2.12 E-12
11	0.0028 64733 3	4.3 6E - 06	4.3 6E - 06	- 0.0069 44290 4	1.23E -10	4.82E -08	- 1.77 E-05	- 1.7 7E- 05	0.0094 12729 2	1.6 4E- 06	- 1.6 4E- 06	- 4.81E -12	- 2.00E -07	1.49E- 06	- 4.98 E-13
12	0.0036 59429	4.2 8E - 06	4.2 8E - 06	- 0.0087 82561 9	- 2.59E -10	4.90E -08	- 2.36 E-05	- 2.3 6E- 05	0.0118 08945	- 8.0 2E- 07	8.0 2E- 07	- 6.29E -10	- 2.70E -07	5.30E- 05	- 1.27 E-13
13	0.0049 48946 2	3.6 0E - 06	3.6 0E - 06	- 0.0117 65971	- 1.89E -10	2.70E -08	- 3.12 E-05	- 3.1 2E- 05	0.0156 97466	- 2.1 1E- 06	2.1 1E- 06	9.73E -11	- 4.36E -07	2.58E- 05	4.81 E-13

14	0.0074 42859 9	9.4 5E - 06	9.4 4E - 06	- 0.0177 42429	3.98E -10	6.26E -08	- 4.96 E-05	- 4.9 6E- 05	0.0237 15939	2.8 5E- 06	- 2.8 5E- 06	- 5.21E -10	- 6.56E -07	3.73E- 05	- 1.46 E-11
15	0.0116 15873	2.2 1E - 05	2.2 1E - 05	- 0.0276 28809	- 8.25E -11	2.92E -07	- 6.61 E-05	- 6.6 1E- 05	0.0362 649	1.5 3E- 05	- 1.5 3E- 05	1.08E -09	- 7.18E -07	1.94E- 04	4.01 E-12

**Table S6:** Broadband (2 $\mu\text{m}$ – 150 $\mu\text{m}$ ) MDL with NA = 0.0998, f = 10 mm

Wavelength (um)	Piston	Ti p	Til t	Defoc us	Verti cal astigmatism	Obliq ue astigmatism	Hori zont al coma	Ver tica l coma	Prima ry spherical	Obl ique tref oil	Ver tica l tref oil	Verti cal secondary astigmatism	Obliq ue secondary astigmatism	Vertic al quadrafoil	Obli que quadrafoil
2.00E-06	3.60E-05	- 4.1 1E - 09	- 4.1 1E - 09	- 8.76E- 05	1.64E- 11	- 4.22E -12	1.98 E-08	1.9 8E- 08	0.0001 04113 95	- 1.2 7E- 09	1.2 7E- 09	4.57E -11	1.53E -11	- 4.50E- 07	7.03 E-15
2.50E-06	3.07E-05	- 1.0 6E - 08	- 1.0 7E - 08	- 6.97E- 05	1.82E- 11	- 2.50E -11	2.12 E-08	2.1 2E- 08	8.54E- 05	- 1.1 8E- 08	1.1 8E- 08	- 2.54E -12	7.99E -12	8.34E- 08	6.31 E-15
3.00E-06	3.34E-05	- 2.7 4E - 08	- 2.7 5E - 08	- 7.13E- 05	3.19E- 12	- 1.45E -11	2.04 E-08	2.0 4E- 08	9.35E- 05	- 2.9 0E- 08	2.9 0E- 08	- 7.25E -12	6.47E -11	1.43E- 07	9.96 E-15
3.50E-06	5.49E-05	5.0 4E - 09	5.0 5E - 09	- 0.0001 18190 89	1.97E -11	1.70E -11	2.33 E-08	2.3 3E- 08	0.0001 49520 42	1.5 5E- 08	- 1.5 6E- 08	- 4.56E -11	- 6.56E -11	3.00E- 07	3.15 E-14
4.00E-06	7.48E-05	- 3.1 0E - 08	- 3.1 0E - 08	- 0.0001 50311 43	8.13E -12	4.30E -11	- 1.70 E-08	- 1.6 9E- 08	0.0001 98224 88	- 2.6 5E- 09	2.6 5E- 09	4.40E -12	- 1.17E -10	- 1.60E- 07	- 1.48 E-14
4.50E-06	7.71E-05	- 9.5 8E - 09	- 9.5 5E - 09	- 0.0001 63423 79	1.19E -11	- 3.13E -10	- 6.19 E-09	- 6.1 8E- 09	0.0001 99717 47	1.7 1E- 09	- 1.7 2E- 09	5.03E -12	- 7.16E -10	- 6.99E- 07	1.32 E-14

5.00E-06	0.0001 13580 57	- 4.5 4E - 08	- 4.5 4E - 08	- 0.0002 52025 81	2.64E-11	1.03E-09	1.46 E-07	1.4 6E- 07	0.0003 15754 85	5.9 8E- 09	- 5.9 6E- 09	- 5.67E- -11	1.93E- -09	- 5.18E- 07	- 7.54 E-14
6.00E-06	0.0002 07064 03	- 9.0 5E - 08	- 9.0 8E - 08	- 0.0004 45359 1	9.53E-11	- 1.03E- -10	3.44 E-07	3.4 4E- 07	0.0005 54587 34	- 2.8 1E- 08	2.8 2E- 08	- 3.90E- -11	3.55E- -10	- 2.05E- 06	- 2.32 E-13
7.00E-06	0.0002 66492 86	- 1.3 6E - 07	- 1.3 7E - 07	- 0.0006 05085 52	1.10E-10	7.25E-10	2.48 E-07	2.4 8E- 07	0.0007 39886 43	- 7.1 9E- 08	7.2 1E- 08	- 1.52E- -11	1.37E- -09	- 2.38E- 06	2.71 E-14
8.00E-06	0.0002 43837 81	- 1.3 2E - 07	- 1.3 3E - 07	- 0.0005 26411 81	3.57E-11	1.36E-09	3.75 E-07	3.7 6E- 07	0.0006 69569 13	7.4 1E- 08	- 7.4 3E- 08	3.98E- -11	2.45E- -09	- 6.79E- 06	2.63 E-13
9.00E-06	0.0004 05949 83	- 2.3 1E - 07	- 2.3 1E - 07	- 0.0009 19758 69	- 4.45E- -12	- 1.95E- -10	5.83 E-07	5.8 4E- 07	0.0011 83807 4	- 4.3 7E- 08	4.3 6E- 08	- 7.83E- -11	3.94E- -10	- 1.23E- 05	1.43 E-13
1.00E-05	0.0004 40991 25	- 2.2 2E - 07	- 2.2 3E - 07	- 0.0009 90925 24	1.02E-10	- 2.21E- -09	5.43 E-07	5.4 3E- 07	0.0012 63190 8	8.6 2E- 08	- 8.6 4E- 08	- 1.72E- -10	- 3.71E- -09	- 1.47E- 05	5.02 E-14
1.10E-05	0.0005 35924 86	- 2.3 4E - 07	- 2.3 5E - 07	- 0.0011 90097	- 1.78E- -11	- 3.59E- -09	7.83 E-07	7.8 4E- 07	0.0016 30180 7	2.2 6E- 07	- 2.2 7E- 07	3.26E- -11	- 6.32E- -09	- 5.20E- 05	1.12 E-13
1.20E-05	0.0004 96431 2	- 2.5 0E - 07	- 2.5 0E - 07	- 0.0011 96168 4	- 4.37E- -11	- 6.92E- -10	6.19 E-07	6.1 9E- 07	0.0016 39573	- 3.9 8E- 09	4.1 2E- 09	- 8.78E- -11	- 9.05E- -10	- 3.21E- 05	4.01 E-13
1.30E-05	0.0005 04706 46	- 3.3 6E - 07	- 3.3 6E - 07	- 0.0012 51628	- 1.00E- -11	- 1.03E- -09	5.18 E-07	5.1 9E- 07	0.0016 59275 6	- 1.2 2E- 07	1.2 3E- 07	- 1.53E- -10	- 9.67E- -10	- 1.26E- 05	- 8.37 E-14
1.40E-05	0.0007 09952 61	- 4.1 6E - 07	- 4.1 7E - 07	- 0.0017	8.88E-11	1.05E-09	9.84 E-07	9.8 4E- 07	0.0022 22884 9	1.2 7E- 09	- 1.3	- 7.87E- -10	2.95E- -09	- 5.29E- 06	1.44 E-13

		-	-	41766							4E-				
		07	07	7							09				
1.50E-05	0.0012607493	8.56E-07	8.57E-07	0.0029816185	2.64E-10	-9.82E-10	2.26E-06	2.26E-06	0.0037503445	-1.48E-07	1.48E-07	1.43E-11	1.30E-09	-3.44E-05	4.14E-13
2.00E-05	0.0012002293	7.69E-07	7.70E-07	0.0029419332	1.85E-10	4.87E-10	1.60E-06	1.60E-06	0.0038537516	-1.09E-07	1.09E-07	-1.19E-11	4.00E-10	-1.31E-06	1.83E-12
2.50E-05	0.0023448709	1.66E-06	1.66E-06	0.0058032391	2.79E-10	-2.42E-09	3.47E-06	3.47E-06	0.0073477505	-4.25E-07	4.25E-07	-8.08E-10	1.44E-09	9.57E-05	-3.20E-13
3.00E-05	0.0034424728	2.61E-06	2.61E-06	0.008157203	7.34E-10	-1.21E-09	7.90E-06	7.89E-06	0.0099418815	-1.56E-10	-2.85E-10	-3.71E-10	9.16E-09	0.00013789303	4.34E-12
3.50E-05	0.0036003364	4.56E-06	4.57E-06	0.0081717176	-1.15E-10	-3.97E-09	7.40E-06	7.39E-06	0.0099516697	-2.26E-06	2.26E-06	1.24E-09	3.59E-09	7.66E-05	1.03E-13
4.00E-05	0.0043393276	4.72E-06	4.72E-06	0.0096239634	2.37E-10	-5.27E-09	7.49E-06	7.49E-06	0.012062714	-1.99E-06	2.00E-06	3.32E-09	-1.16E-08	2.75E-06	-7.50E-12
4.50E-05	0.0064581926	5.33E-06	5.33E-06	0.014184326	-1.49E-10	1.29E-09	3.83E-06	3.83E-06	0.018753756	-2.07E-06	2.07E-06	7.03E-10	-3.40E-08	-0.00018034986	1.17E-11
5.00E-05	0.011248727	2.95E-06	2.95E-06	0.025116773	9.12E-10	2.91E-08	-9.82E-07	-9.78E-07	0.03454797	2.32E-06	2.32E-06	-1.54E-09	-5.13E-08	0.00044698146	4.81E-11
6.00E-05	0.027711842	1.26E-05	1.26E-05	0.063778833	8.90E-09	4.77E-08	-3.29E-05	-3.29E-05	0.089453511	1.72E-05	1.73E-05	-1.29E-11	-2.36E-07	-0.00086950965	1.33E-11

7.00E-05	0.03307379	1.84E-05	1.85E-05	-0.077880569	7.27E-09	2.09E-08	-6.62E-05	-6.62E-05	0.10969856	2.13E-05	-2.14E-05	-1.51E-08	-3.93E-07	0.00021952733	8.12E-11
8.00E-05	0.038954012	2.73E-05	2.74E-05	-0.094490349	4.74E-09	8.51E-08	-7.45E-05	-7.45E-05	0.13149491	3.59E-05	-3.59E-05	-2.33E-08	-3.53E-07	0.0023152409	-9.47E-11
9.00E-05	0.030772073	1.86E-05	1.86E-05	-0.074431442	1.60E-08	6.71E-08	-6.26E-05	-6.26E-05	0.10226212	1.71E-05	-1.72E-05	2.95E-08	-2.35E-07	0.0035452121	4.53E-11
0.0001	0.027050912	1.52E-05	1.52E-05	-0.066132225	1.69E-08	5.89E-08	-5.59E-05	-5.59E-05	0.090980023	1.10E-05	-1.10E-05	-1.15E-08	-1.81E-07	0.0044395276	4.03E-12
0.00011	0.026356924	1.73E-05	1.73E-05	-0.063480824	4.42E-08	6.44E-08	-4.66E-05	-4.66E-05	0.085929327	1.38E-05	-1.38E-05	8.97E-09	-1.39E-07	0.0053840363	-7.69E-11
0.00012	0.026124706	1.57E-05	1.57E-05	-0.063553244	1.58E-08	4.76E-08	-3.78E-05	-3.78E-05	0.086945102	1.04E-05	-1.05E-05	-1.39E-07	-1.10E-07	0.0058447546	6.57E-11
0.00013	0.026890904	1.55E-05	1.55E-05	-0.065207154	3.11E-08	4.71E-08	-4.02E-05	-4.02E-05	0.089368679	6.37E-06	-6.38E-06	-6.11E-08	-8.42E-08	0.0073220516	-1.24E-10
0.00014	0.028860269	1.56E-05	1.56E-05	-0.068073899	1.13E-08	4.29E-08	-4.77E-05	-4.77E-05	0.091637485	4.10E-06	-4.09E-06	2.37E-09	-9.24E-08	0.0090332562	-4.24E-11
0.00015	0.031044755	1.40E-05	1.40E-05	-0.071999855	4.75E-08	3.99E-08	-5.19E-05	-5.19E-05	0.095432326	2.89E-06	-2.90E-06	4.99E-08	-9.25E-08	0.010147722	3.08E-11

### 8. Distortion analysis for measured wavefront of broadband (450 nm – 850 nm) MDL

The following optical setup, shown in Fig. S14 was constructed to measure the geometric distortion, vignetting and signal-to-noise ratio (SNR) of the VIS/NIR MDL. A screen with different patterns used for the different experiments was placed 115 mm away from the MDL, which in turn was placed in front of a sensor. Two white LEDs illuminate the screen from far away, so that the screen may be uniformly illuminated [25].



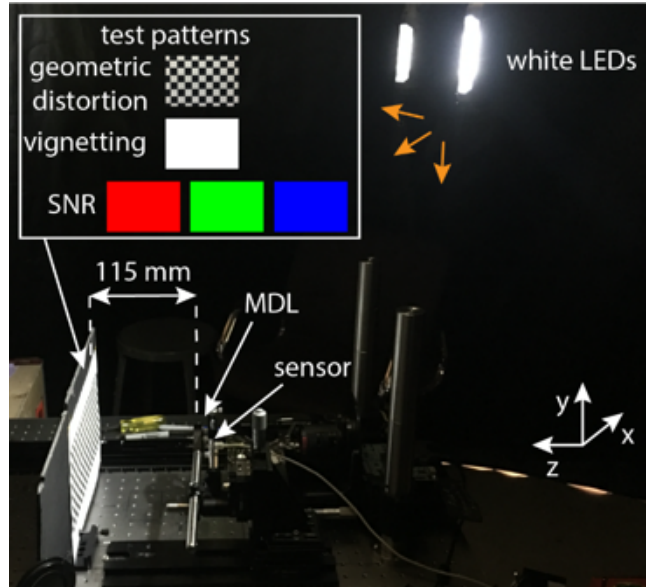


**Fig. S17:** Optical setup used to measure the geometric distortion, vignetting and signal-to-noise ratio (SNR) of a test VIS/NIR multi-level diffractive lens.

## 9. Illumination Spectrum Details

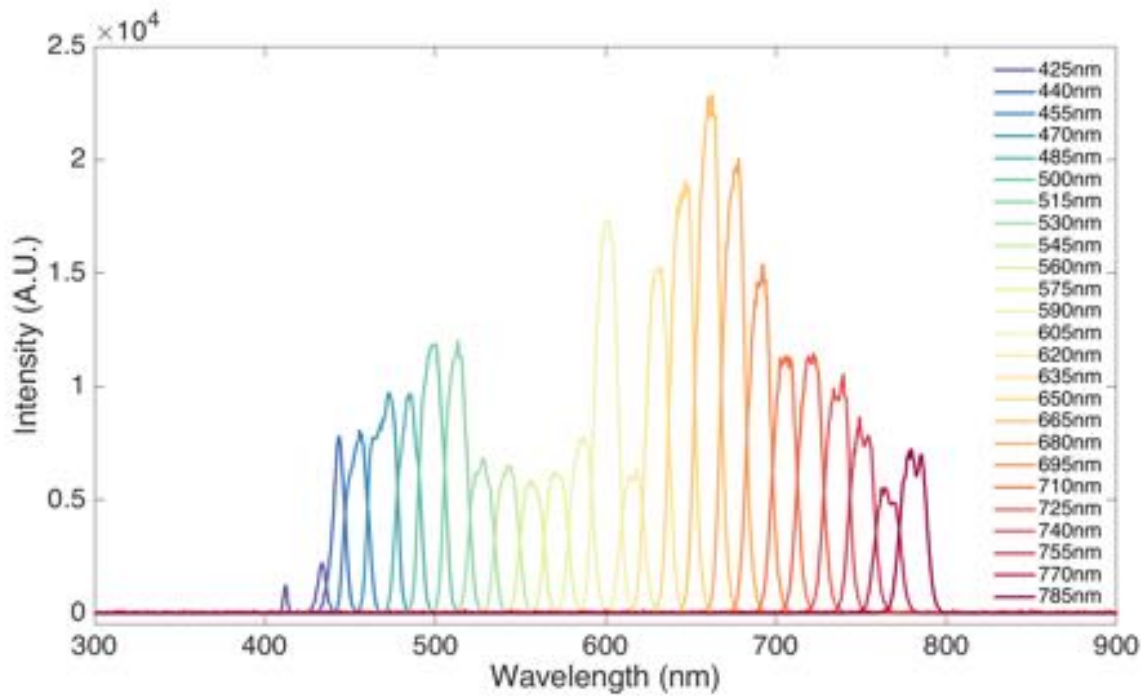


**Fig. S18:** Spectrum of SuperK Varia. For each wavelength, the bandwidth is 15 nm. The envelope of all these wavelengths is the full broadband.

## 10. MDL achromatic from 0.5mm to 15mm

### 10.1 Simulated scalar Point Spread Functions (PSFs)

The scalar simulated point spread functions (PSFs) for the broadband lens designed in AZ9260 are provided below:

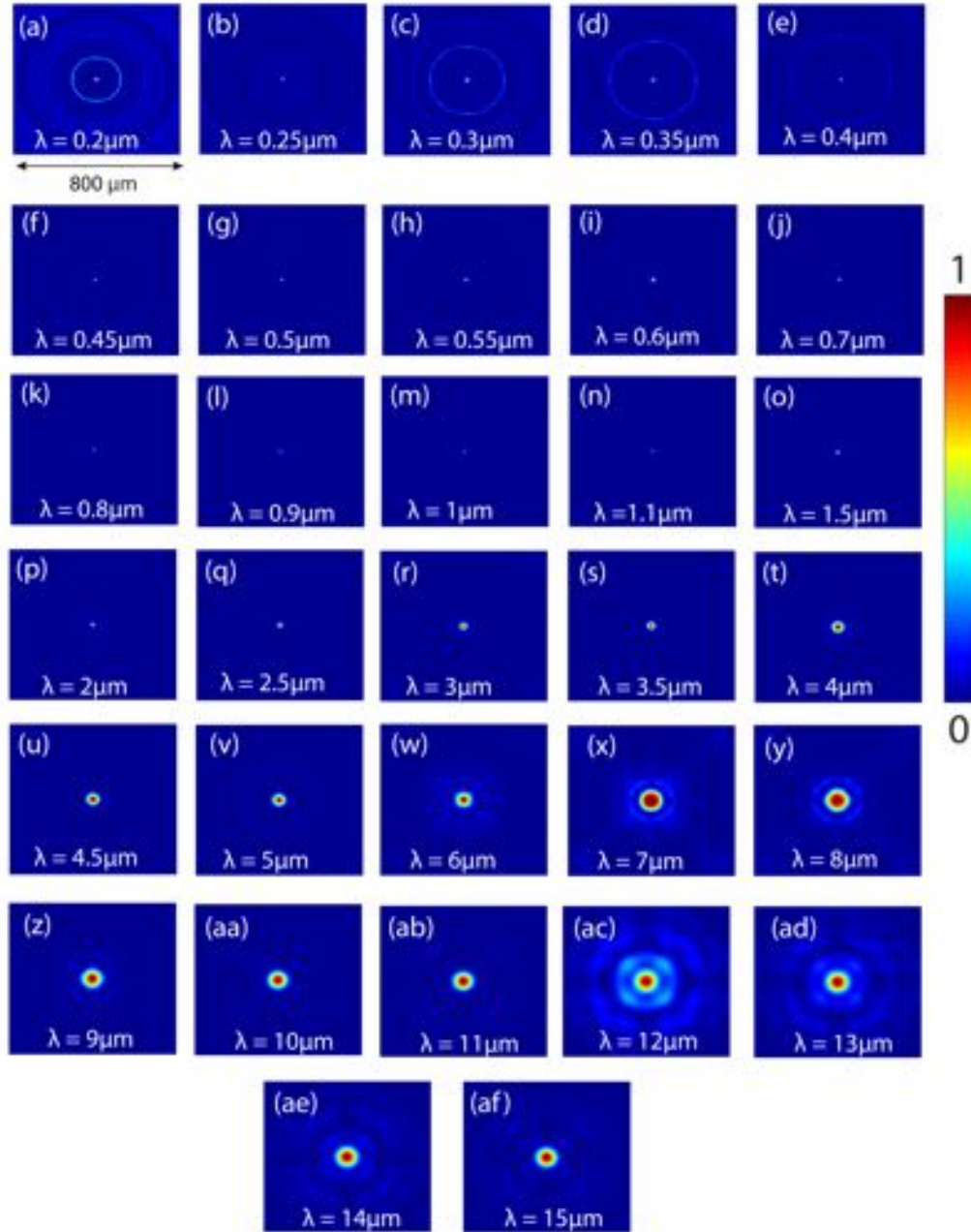


**Fig. S19:** Simulated PSFs for (a)  $0.2\mu\text{m}$  (b)  $0.25\mu\text{m}$  (c)  $0.3\mu\text{m}$  (d)  $0.35\mu\text{m}$  (e)  $0.4\mu\text{m}$  (f)  $0.45\mu\text{m}$  (g)  $0.5\mu\text{m}$  (h)  $0.55\mu\text{m}$  (i)  $0.6\mu\text{m}$  (j)  $0.7\mu\text{m}$  (k)  $0.8\mu\text{m}$  (l)  $0.9\mu\text{m}$  (m)  $1\mu\text{m}$  (n)  $1.1\mu\text{m}$  (o)  $1.5\mu\text{m}$  (p)  $2\mu\text{m}$  (q)  $2.5\mu\text{m}$  (r)  $3\mu\text{m}$  (s)  $3.5\mu\text{m}$  (t)  $4\mu\text{m}$  (u)  $4.5\mu\text{m}$  (v)  $5\mu\text{m}$  (w)  $6\mu\text{m}$  (x)  $7\mu\text{m}$  (y)  $8\mu\text{m}$  (z)  $9\mu\text{m}$  (aa)  $10\mu\text{m}$  (ab)  $11\mu\text{m}$  (ac)  $12\mu\text{m}$  (ad)  $13\mu\text{m}$  (ae)  $14\mu\text{m}$  and (af)  $15\mu\text{m}$ .

## 10.2. Simulated FWHM

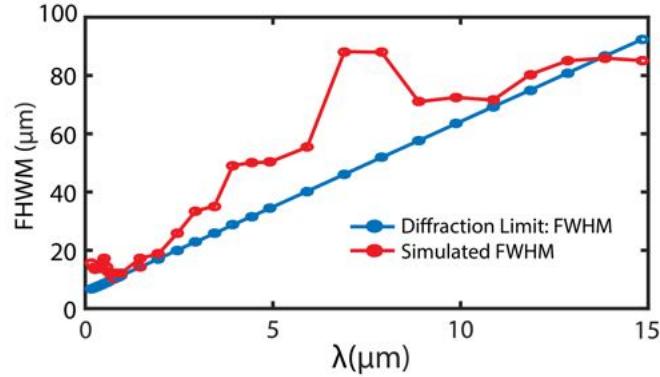


*Fig. S20: FWHM. plot of the 0.5 $\mu\text{m}$  – 15 $\mu\text{m}$  broadband MDL.*

### 10.3. 2D FDTD Simulation Setup and Simulated z-propagation plot of the 0.5 $\mu\text{m}$ – 15 $\mu\text{m}$ broadband MDL

The 2D full wave FDTD simulations were carried out using Lumerical FDTD Solutions. The material properties (refractive index and absorption coefficient as a function of frequency) of the Photoresist (AZ9260) was imported into Lumerical directly as the structure’s optical data. A “.lsf” script was written to replicate the lens geometry using the same dimensions, which was specified during the optimization process as depicted in Fig. S20(a). An incident plane wave (type: diffracting) along the backward “y-axis” direction illuminated the diffractive lens surface. For the broadband excitation, the entire range or bandwidth of the pulse was defined for the appropriate design.

The entire FDTD simulation region was considered from the back surface of the spherical lens right up to roughly  $\sim 1.5$  times the distance from the focal plane. A Perfectly Matched Layer (PML) boundary condition set up. Due to the inherent symmetry of the designed structure, the x-min boundary was set to “anti-symmetric” which reduced the requirements by 1/2 of the original simulation requirements in terms of both time and memory. The default mesh was used to simulate the structures instead of a very fine mesh to avoid the huge computation time. The mesh accuracy was kept at “4” which has a good tradeoff for precision and accuracy versus the time and memory requirement. Field monitors placed to observe the field profiles of the propagating electromagnetic radiation.

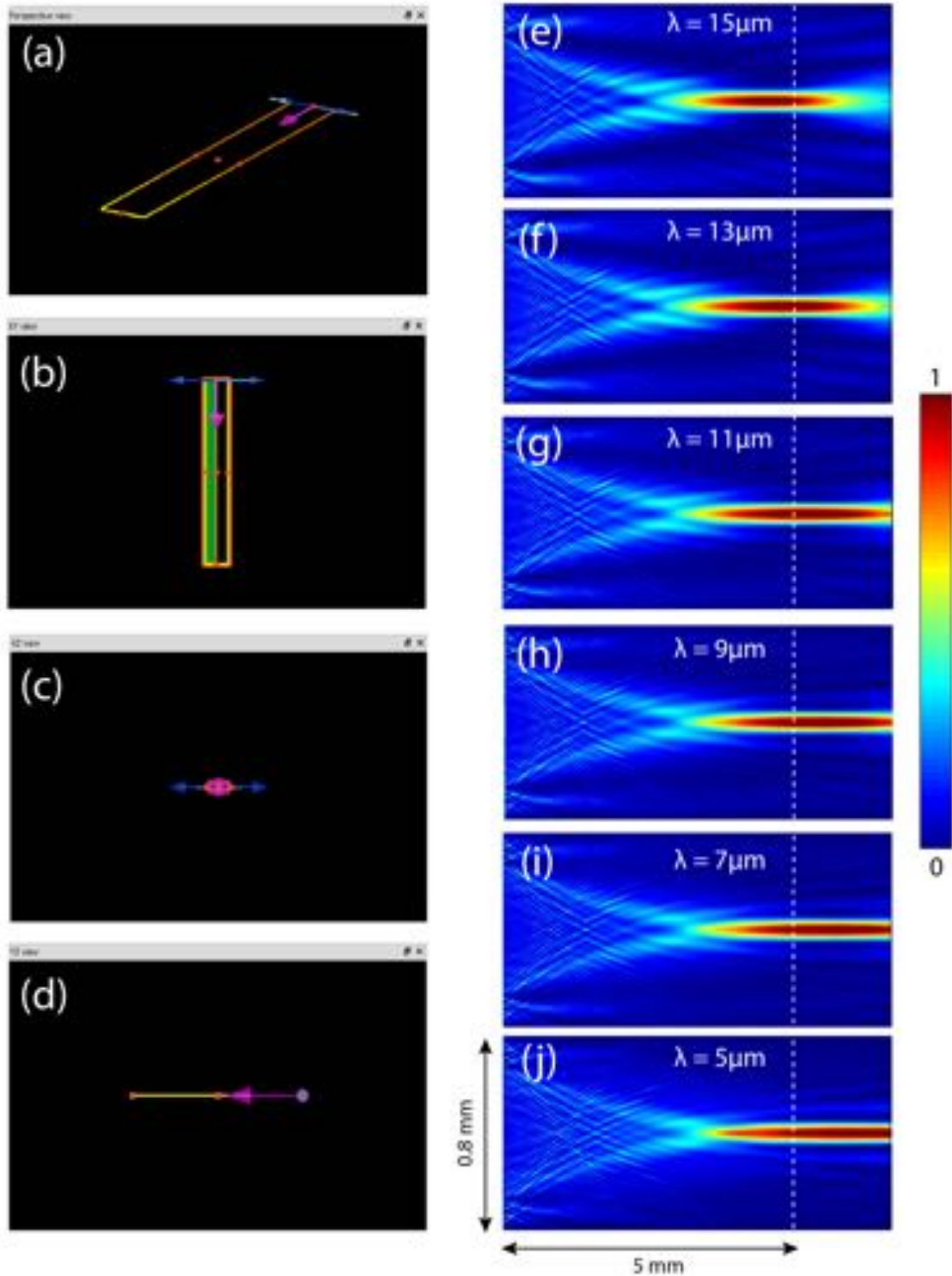


**Fig. S21:** 2D FDTD simulation setup showing the (a) perspective view, (b) XY view, (c) XZ view and (d) YZ view in Lumerical FDTD solutions. Simulated z-propagation plot for (e) 15 $\mu\text{m}$  (f) 13 $\mu\text{m}$  (g) 11 $\mu\text{m}$  (h) 9 $\mu\text{m}$  (i) 7 $\mu\text{m}$  (j) 5 $\mu\text{m}$ .

### 11. Impact of degrees of freedom on 0.5 $\mu\text{m}$ to 15 $\mu\text{m}$ MDL performance.

### 11.1. Effect of pixel width

We simulated the effect of both larger and smaller pixel width keeping the number of pixel height levels fixed at 100 in the design. We observed that the efficiency was almost constant across the range of 6 $\mu\text{m}$  to 10  $\mu\text{m}$ ; after which we see that the average efficiency fall by a margin of about  $\sim 15\%$  when the pixel width was even increased to 12  $\mu\text{m}$  and finally at 14 $\mu\text{m}$  the efficiency drops bellows 60%.

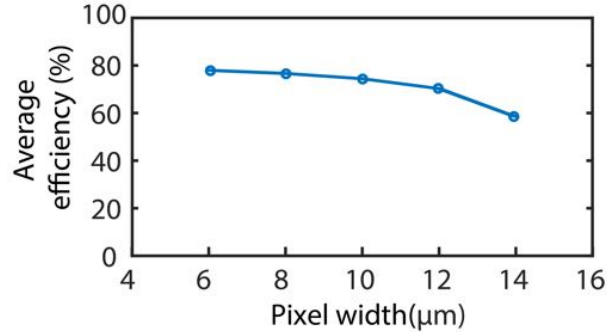


*Fig. S22: Effect of pixel width on average efficiency of the 0.5 $\mu\text{m}$  – 15 $\mu\text{m}$  broadband MDL.*

### 11.2. Effect of number of height levels

We simulated the effect of both larger and smaller number of pixel height levels keeping the width of each individual pixel at 8 $\mu\text{m}$  in the design. We observed that the efficiency increased by a substantial margin from 8 pixels levels to 64 pixels levels. After that, the increase the average efficiency was almost constant from 64 to 128 pixels. Hence, the use of 100 pixels was a good choice from a design perspective.

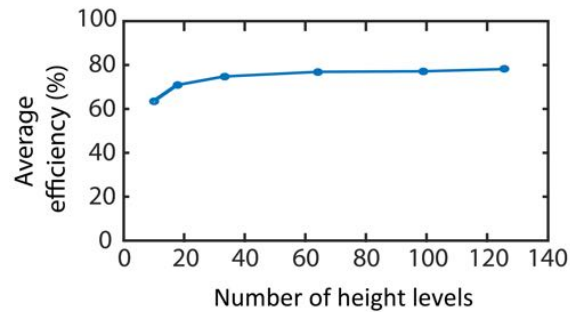


*Fig. S23: Effect of the number of height levels on average efficiency of the 0.5 $\mu\text{m}$  – 15 $\mu\text{m}$  broadband MDL.*

## 12. Performance of an MDL achromatic over 2.5 $\mu\text{m}$ to 150 $\mu\text{m}$ .

### 12.1. Simulated scalar Point Spread Functions (PSFs)

The scalar simulated point spread functions (PSFs) for the broadband lens designed in silicon are provided below:

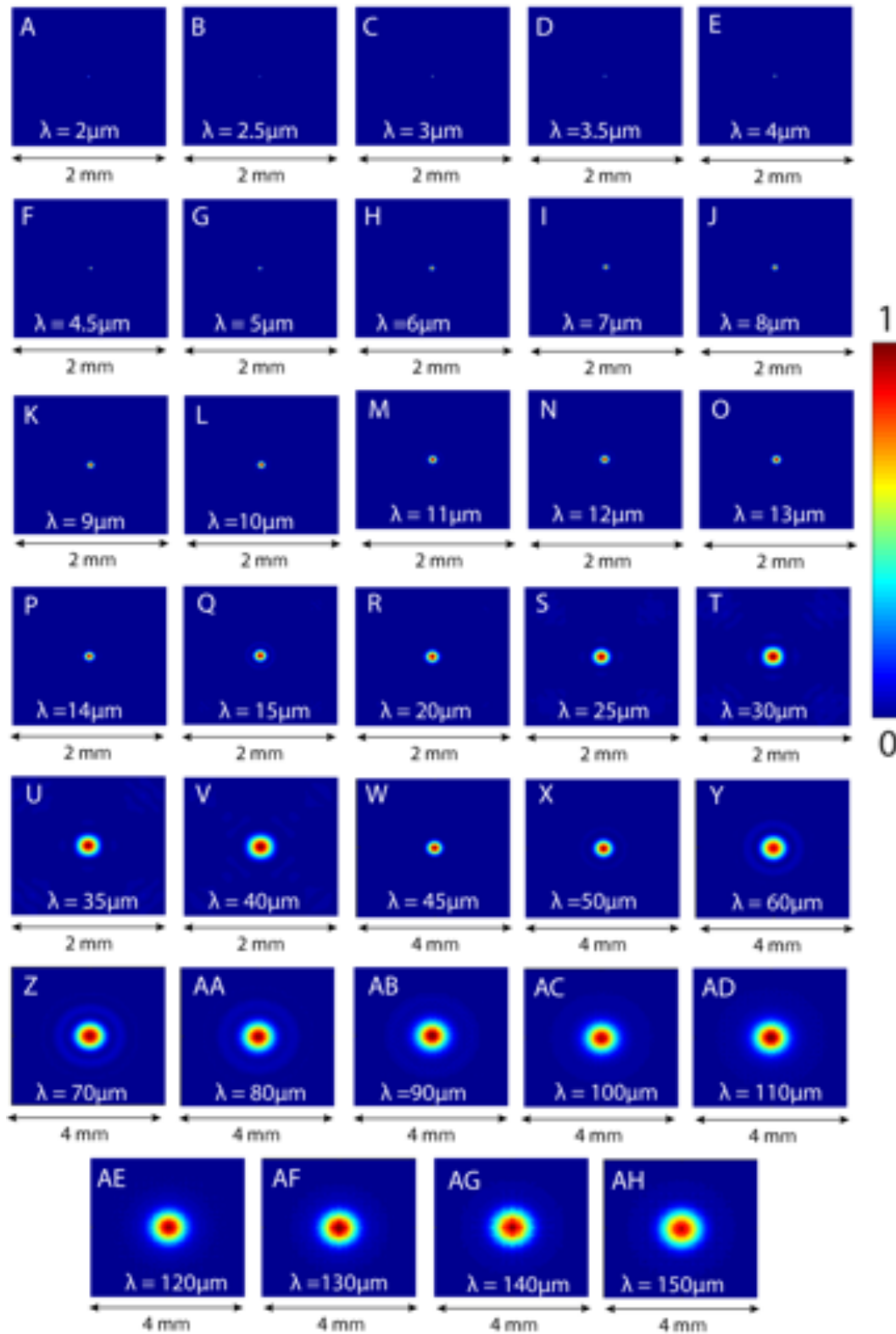


**Fig. S24:** Simulated PSFs for (a) 2um (b) 2.5um (c) 3um (d) 3.5um (e) 4um (f) 4.5um (g) 5um (h) 6um (i) 7um (j) 8um (k) 9um (l) 10um (m) 11um (n) 12um (o) 13um (p) 14um (q) 15um (r) 20um (s) 25um (t) 30um (u) 35um (v) 40um (w) 45um (x) 50um (y) 60um (z) 70um (aa) 80um (ab) 90um (ac) 100um (ad) 110um (ae) 120um (af) 130um (ag) 140um and (ah) 150um.

## 12.2. FWHM

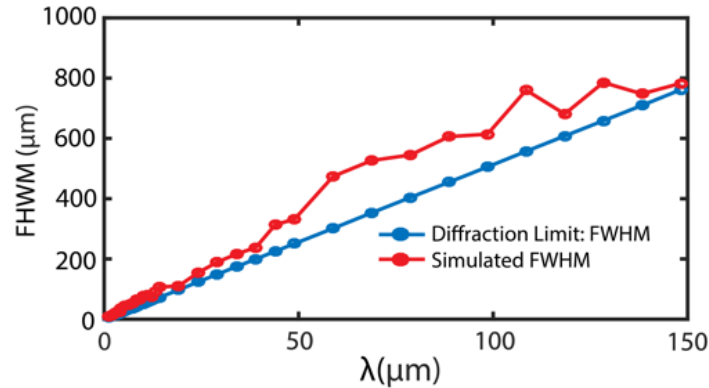


**Fig. S25:** FWHM plot of the 2.5um – 150um broadband MDL.

## Reference

- [1] S. Shrestha, A. Overvig, M. Lu, A. Stein, N. Yu, “Broadband achromatic dielectric metalenses” *Light: Sci. Appl.* 2018, 7, 85.
- [2] S. Wang, P.C. Wu, V.C. Su, Y.C. Lai, M.K. Chen, H.Y. Kuo, B.H. Chen, Y.H. Chen, T.T. Huang, J.H. Wang, and R.M. Lin, “A broadband achromatic metalens in the visible.” *Nat. Nano.*, 13(3), p.227 (2018).
- [3] M. Khorasaninejad, F. Aieta, P. Kanhaiya, M.A. Kats, P. Genevet, D. Rousso, and F. Capasso, “Achromatic metasurface lens at telecommunication wavelengths.” *Nano lett.* 15(8), pp.5358-5362 (2015).
- [4] S. Wang, P.C. Wu, V.C. Su, Y.C. Lai, C.H. Chu, J.W. Chen, S.H. Lu, J. Chen, B. Xu, C.H. Kuan, and T. Li, “Broadband achromatic optical metasurface devices.” *Nat. comm.*, 8(1), p.187 (2017).
- [5] W.T. Chen, A.Y. Zhu, V. Sanjeev, M. Khorasaninejad, Z. Shi, E. Lee, and F. Capasso, “A broadband achromatic metalens for focusing and imaging in the visible.” *Nat. Nano.*, 13(3), p.220 (2018).
- [6] Z. Lin, B. Groever, F. Capasso, A.W. Rodriguez, and M. Lončar, “Topology-Optimized Multilayered Metaoptics.” *Phys. Rev. Appl.*, 9(4), p.044030 (2018).
- [7] M. Ye, V. Ray, and Y.S. Yi, “Achromatic Flat Subwavelength Grating Lens Over Whole Visible Bandwidths.” *IEEE Phot. Tech. Lett.*, 30(10), pp.955-958 (2018).
- [8] J. Hu, C.H. Liu, X. Ren, L.J. Lauhon, and T.W. Odom, “Plasmonic lattice lenses for multiwavelength achromatic focusing.” *ACS nano*, 10(11), pp.10275-10282 (2016).
- [9] Z. Shi, M. Khorasaninejad, A.Y. Zhu, W.T. Chen, V. Sanjeev, A. Zaidi, and F. Capasso, “Achromatic Metalens over 60 nm Bandwidth in the Visible.” In *CLEO: QELS\_Fundamental Science* (pp. FM1H-2) (2017).
- [10] S. Wang, C. Zhou, Z. Liu, and H. Li, “Design and analysis of broadband diffractive optical element for achromatic focusing.” In *Holography, Diffractive Optics, and Applications VII* (Vol. 10022, p. 100221J) (2016).
- [11] W. T. Chen, A.Y. Zhu, J. Sisler, Z. Bharwani, and F. Capasso, “A broadband achromatic polarization-insensitive metalens consisting of anisotropic nanostructures.” *arXiv preprint arXiv:1810.05050* (2018).
- [12] H. Zheng, J. Ding, L. Zhang, H. Lin, S. An, T. Gu, H. Zhang, and J. Hu, “Ultra-thin, high-efficiency mid-infrared Huygens metasurface optics.” In *2018 International Applied Computational Electromagnetics Society Symposium (ACES)* (pp. 1-2). IEEE (2018).
- [13] S. Zhang, A. Soibel, S.A. Keo, D. Wilson, S. Rafol, D.Z. Ting, A. She, S.D. Gunapala, and F. Capasso, “Solid-Immersion Metalenses for Infrared Focal Plane Arrays.” *arXiv preprint arXiv:1805.06608* (2018).
- [14] H. C. Wang, C.H. Chu, P.C. Wu, H. H. Hsiao, H.J. Wu, J. - W. Chen, W.H. Lee, Y. C. Lai, Y. W. Huang, M.L. Tseng, S. W. Chang, D.P. Tsai, “Ultrathin Planar Cavity Metasurfaces” *Small*, 14, 1703920 (2018).

- [15] H. Zuo, D.Y. Choi, X. Gai, P. Ma, L. Xu, D.N. Neshev, B. Zhang, and B. Luther - Davies, "High - Efficiency All - Dielectric Metalenses for Mid - Infrared Imaging." *Adv. Opt. Mat.*, 5(23), p.1700585 (2017).
- [16] J. Hu, C.H. Liu, X. Ren, L.J. Lauhon, and T.W. Odom, "Plasmonic lattice lenses for multiwavelength achromatic focusing." *ACS nano*, 10(11), pp.10275-10282 (2016).
- [17] Y. Liang, H. Liu, F. Wang, H. Meng, J. Guo, J. Li, and Z. Wei, "High-Efficiency, Near-Diffraction Limited, Dielectric Metasurface Lenses Based on Crystalline Titanium Dioxide at Visible Wavelengths" *Nanomaterials*, 8(5) (2018).
- [18] McKenna, Curt, Kevin Walsh, Mark Crain, and Joseph Lake. "Maskless Direct Write Grayscale Lithography for MEMS Applications." In *Micro/Nano Symposium (UGIM), 2010 18th Biennial University/Government/Industry*, pp. 1-4. IEEE, 2010.
- [19] Wang, Peng, Jose A. Dominguez-Caballero, Daniel J. Friedman, and Rajesh Menon. "A new class of multi-bandgap high-efficiency photovoltaics enabled by broadband diffractive optics." *Progress in Photovoltaics: Research and Applications* 23, no. 9 (2015): 1073-1079.
- [20] Data sheet of Heidelberg  $\mu$ PG 101: <http://www.himt.de/index.php/upg-101.html>
- [21] Data sheet of SuperK Extreme: <http://www.nktphotonics.com/wp-content/uploads/2015/05/superk-extreme.pdf>
- [22] Data sheet of SuperK Varia Filter: [http://www.nktphotonics.com/wp-content/uploads/2015/03/SuperK\\_VARIA.pdf](http://www.nktphotonics.com/wp-content/uploads/2015/03/SuperK_VARIA.pdf)
- [23] <https://www.thorlabs.com/drawings/df3b6b46ef30681e-4FCA62B7-EC91-A58F-DC63FFA3291FEB77/WFS150-7AR-Manual.pdf>
- [24] Platt, Ben C.; Shack, Ronald (October 2001). "History and Principles of Shack-Hartmann Wavefront Sensing". *Journal of Refractive Surgery*. 17(5): S573–7.
- [25] <https://www.edmundoptics.com/resources/application-notes/imaging/distortion/>
- [26] D. F. Edwards and E. Ochoa, "Infrared Refractive Indexes of Silicon," *Appl. Opt.*, **19**, 4130-4131 (1980).
- [27] C. M. Randall and R. D. Rawcliffe, "Refractive indices of Germanium, Silicon and Fused Quartz in the far infrared," *Appl. Opt.* 6(11), 1889-1895 (1967).